CHAPTER 5

Homo- and Heterojunction Interfacial Workfunction Internal Photo-Emission Detectors from UV to IR

A. G. U. Perera*

Contents

* Email: uperera@gsu.edu, Tel: (404)413-6037, Fax: (404)413-6025

Semiconductors and Semimetals, Volume 84
ISSN 0080-8784, DOI: 10.1016/B978-0-12-381337-4.00005-X

© 2011 Elsevier Inc.
All rights reserved.

1. INTRODUCTION

1.1. Introduction to infrared detectors

Infrared (IR) radiation was discovered accidently by Sir Frederick William Herschel (1738–1822), a musician and an astronomer who also discovered the Uranus. Since then, various types of IR detectors were studied (Case, 1917; Johnson, 1983; Levinstein, 1965; Rogalski, 2005; Sclar, 1976). Initial efforts focused on detectors based on thermal effects, the thermometers (Herschel, 1800), and the bolometers which are sensitive to all IR wavelengths but with low sensitivity. The Second World War dramatically increased the interest in IR detection in which photon detectors were developed to improve the performance. Various extrinsic semiconductor (e.g., Si:P and Ge:Zn) photon detectors were developed to extend the detection wavelength beyond the wavelength of intrinsic photoconductors (Kruse, 1981). Doped materials, e.g., germanium doped with copper, zinc, or gold (Levinstein, 1965), demonstrated sensitivities in the long-wavelength infrared (LWIR) range (8–14 μm) and the far infrared (FIR) region. Novel growth techniques such as molecular beam epitaxy (MBE; Cho (1979)) and metal organic chemical vapor deposition (MOCVD; Manasevit (1968)) in the twentieth century allowed band-gap tailoring to develop novel IR detectors that transformed the detector technologies. Now the infrared detectors are used in various sectors not only in defense and security but also in manufacturing, medicine, environment, and various other testing/monitoring applications.

In this chapter, the focus is on detection using internal photoemission across an interfacial workfunction in a semiconductor homo- or a heterojunction architecture. Although quantum well structures also have a junction and an interface, the energy difference between the two states associated with the transitions are because of the quantization effects in the well material but not at an interface. The detector concepts discussed here can be applied to any semiconductor material where an interface can be formed. Varying the interfacial workfunction will lead to different energy photons to be detected giving rise to different threshold wavelength (λ_t) detectors. This idea will be extended to show how multiband detection is achieved in a single detector element. In addition, controlling the operating temperature and the responsivity by adjusting the interfacial workfunction will also be discussed in connection with the spin-orbit

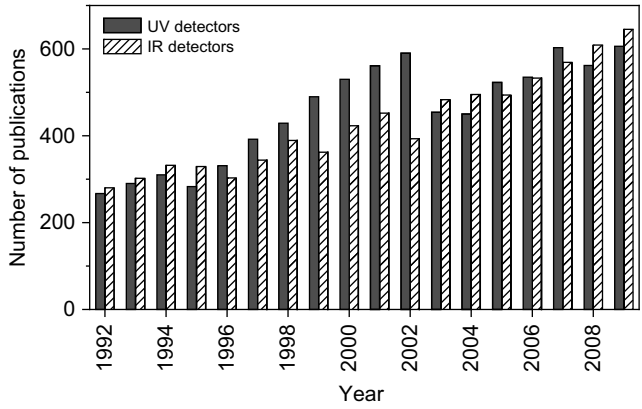

FIGURE 5.1 Number of journal publications reported in each year (January to December) as of July 2009 based on a search in the ISI Web of Knowledge database on the term "UV detector(s)" and "IR detector(s)" in the "topic" field.

split-off detectors. A search on the term "UV detector(s)" and "IR detector(s)" in the "topic" of the ISI Web of Knowledge journals indicated a trend showing increasing interest with more than 200 articles per year, published throughout the period as shown in Fig. 5.1. In the last decade, on average, more than one article per day was published which has "UV detector(s)" or "IR detector(s)" in the title. Hence, this clearly shows that the detector development efforts are still continuing in earnest.

1.2. Semiconductor junctions

In semiconductor physics a junction is formed when two materials are in contact. The term junction refers to the boundary interface where the two semiconductors meet. If the two materials with the same band gap are in contact, what is known as a homojunction is formed. However, these two materials can still have differences such as a *p*-type material and an *n*-type material forming a *p–n* junction or an *n–p–n* transistor. This development has been the dawn of the semiconductor age starting with Bardeen, Schokley, and Brattain discovery, leading to a Nobel Prize (Bardeen, 1956).

When the two materials have different band gaps, the junction is termed a heterojunction. The advent of the novel growth techniques, such as MBE (Cho, 1979) and MOCVD (Manasevit, 1968), and so on, has lead to the development of various heterojunction devices revolutionizing the semiconductor industry. These techniques allow sharp abrupt junctions of various different material systems, leading to various semiconductor devices, e.g., semiconductor lasers, solar cells, detectors, transistors, and

so on. One of the significant factors is actually the band offset, which is produced by the difference in either the doping levels in two materials composing a homojunction and/or the band gaps in a heterojunction. The carriers will see a band-offset when transporting across a homo- or hetero-semiconductor junction. Under illumination, the carriers can excite into higher energy states giving a higher probability to pass through the energy barrier. The use of homo- or heterojunctions with a doped emitter leads to a (photocurrent) response to the incident light because of photon absorption in the emitter and escape across the barrier. The collection of excited carriers confirms the detection of the incoming photon. Adjusting the energy barriers can tailor the detection wavelength. Detector development including a variety of spectral ranges will be discussed in this chapter.

1.3. Internal and external photoemission

Photoemission, first observed and documented by Hertz in 1887, has been recognized as an important step in the development of devices, earning Albert Einstein the Nobel prize in 1929 for his work on external photoemission, which is also known as photoelectric effect (Einstein, 1905). In the classic photoelectric effect, the photons gets absorbed and the energized carriers come out or get ejected from matter and hence can be classified as external photoemission. In this process, there is a threshold energy that is needed to eject the carriers out. With higher incident energy of the light, carriers will also have a higher energy. Once the photons are absorbed, the carriers come out from the original state and overcome an energy barrier but still stay in the material. Then it can be categorized as internal photoemission. For the carriers to come out of the original state, there is a specific energy requirement, which is historically known as the work-function (http://hyperphysics.phy-astr.gsu.edu/hbase/mod2.html). At a semiconductor junction, there is also an interface, which is the boundary between the two sections. In general, there is an energy gap between the two materials which could either be resulting from the band gap difference in the case of a heterojunction or band offset coming from band gap narrowing because of doping the material or a combination of the two. This energy gap at the interface of the two semiconductors can be used to detect photons by matching that energy difference with the incoming photons which in turn will provide the required energy for the carriers to overcome the energy gap. The photoexcited carriers, if collected by the collector, provide the photocurrent, whereas thermally excited carriers will give rise to the dark current which is not useful in the detection and usually needs to be kept low. However, a dark current also plays a role in replenishing the depleted carriers which also allows the detector to operate continuously.

2. FREE CARRIER–BASED INFRARED DETECTORS

Internal photoemission (IP) detectors were first proposed by Shepherd *et al*. (1971) in Schottky barrier structures. Since then, several different types of internal photoemission detectors have been demonstrated (Perera, 2001; Perera *et al.*, 1995; Shepherd, 1992). Among them are metal-semiconductor Schottky barrier IR detectors, such as PtSi/Si detectors (Kosonocky, 1992) operating in 3–5 μm range; semiconductor heterojunction IR detectors, Ge_xSi_{1-x}/Si detectors (Lin and Maserjian, 1990; Tsaur *et al.*, 1991) developed for 8–14 μm or even longer wavelengths; and a degenerate Si homojunction detector (Tohyama *et al.*, 1991), which has a response in the 1–7 μm range. The absorber and photoemitter can be a metal, a metal silicide, or a degenerate semiconductor in the Schottky barrier, silicide, and degenerate homojunction detectors, respectively. A similar detector concept was proposed and demonstrated by Liu *et al.* (1992), using Si MBE multilayer structures in the long-wave infrared (LWIR) range. However, the basic operating mechanism is the same, and following the terminology of Lin and Maserjian (1990), all of these detectors including the free carrier–based detectors can be described as Heterojunction or Homojunction Internal Photoemission (HIP) detectors.

2.1. Types of HIP detectors

A basic HIP detector consists of a doped emitter layer and an undoped barrier layer. In the homojunction detectors, the absorber/photoemitter will be a doped semiconductor. The doping will cause the bandgap to narrow, forming a barrier at the interface with an undoped layer of the same material. The height and the shape of the barrier will depend on the doping level in the HIP, which can be divided into three types (type-I, -II, and -III; Perera and Shen (1999); Perera *et al.* (1995)). These basic types of detectors operate similarly for both *n*- and *p*-doping (except for the carriers; electrons in *n*-type and holes in *p*-type) and will be described here for *p*-type detectors. Significant effective band-gap shrinkage has been observed for heavily doped *p*-type Si (Dumke, 1983), Ge (Jain and Roulston, 1991), and GaAs (Harmon *et al.*, 1994). Better carrier-transport properties of GaAs such as higher mobility will translate into a higher gain, which may produce improved performance for these types of detectors. In the heterojunction case, the only difference is the use of different bandgap materials for the emitter and barrier, which will introduce an additional component for barrier formation.

2.1.1. Type I HIP detectors: $N_a < N_c$ ($E_F > E_v^{p^+}$)

The type I detectors are characterized by an acceptor doping concentration (N_a) in the p^+-layer high enough to form an impurity band but still

less than the Mott critical value (N_c), so the Fermi level (E_F) is located in the impurity band at low temperatures. The incident FIR light is absorbed by impurity photo-ionization, with a threshold workfunction given by $\Delta = E_F - E_v^{p^+}$, where $E_v^{p^+}$ is the valence band edge in the p^+-layer. The photoexcited holes are collected by an electric field formed in the *i*-layer because of an external bias. Type I HIP detectors are analogous to semiconductor photoemissive detectors (Escher, 1981) in their operation, which can be described by a three-step process (see Fig. 5.2A): (1) holes are photoexcited from impurity band states into valence band states; (2) phonon relaxation rapidly thermalizes the photoexcited holes to the top of the valence band, and then diffuses to the emitter/barrier interface, with the transport probability determined by the hole diffusion length; and (3) the holes tunnel through an interfacial barrier (ΔE_v), which is because of the offset of the valance band edge caused by the bandgap-narrowing effect and are collected by the electric field in the *i*-region. The collection efficiency will depend on the tunneling probability and hence on the *i*-region electric field. The threshold wavelength (λ_t) can be tailored with the doping concentration to some extent because with the increase

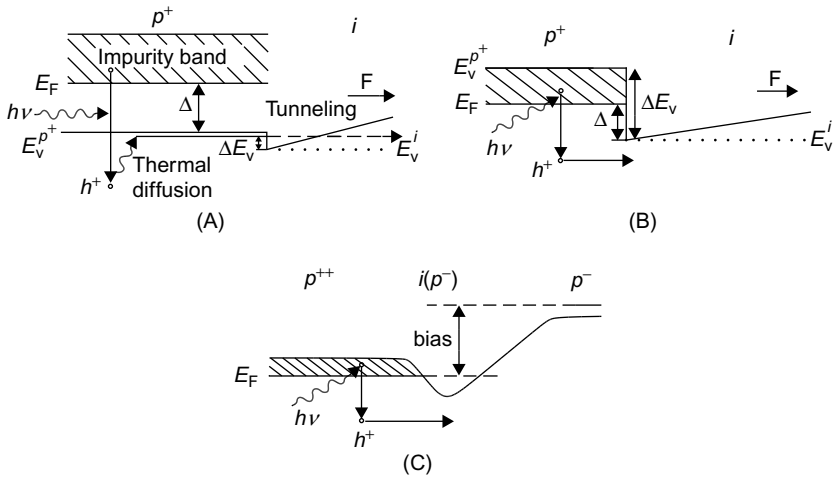

FIGURE 5.2 Energy band diagrams for the three different types of HIP detectors for the p-doped case. (A) Type I: $N_a < N_c (E_F > E_v^{p^+})$; (B) Type II: $N_c < N_a < N_0$ $(E_v^{p^+} > E_F > E_v^i)$; (C) Type III: $N_a > N_0$ $(E_F < E_v^i)$. Here, N_c is the Mott critical concentration and N_0 is the critical concentration corresponding to $\Delta = 0$. In (A) and (B), the valence band edge of the *i*-layer is represented by a dotted line for $V_b = V_0$ (flatband) and by a solid line for $V_b > V_0$.
Reused with permission from Perera (2001). Copyright 2001, Academic Press.

of doping concentration, the impurity band broadens and the band edge moves rapidly toward the valance band (Jain *et al.*, 1991).

The impurity compensation effect (Perera *et al.*, 1995), which was neglected in the previous discussion, can induce an electric field in the p^+-layer. This field may extend over a wide region of the p^+-layer for very small compensating concentrations. This is the case of blocked-impurity-band (BIB) detectors (Petroff and Stapelbroek, 1986; Szmulowicz and Madarasz, 1987), for which the photoexcited carrier–collection mechanisms ((2) and (3) above) are replaced by field-induced sweep out of the carriers. In contrast to the type I HIP detector, the BIB detector resembles a reverse-biased photovoltaic detector in its operation, with the collection efficiency in the electric field region approaching 100%. However, if the compensated acceptor concentration is high in the majority of the p^+-layer, there is no electric field induced when an external voltage is applied, except for a very small depletion region near the p^+-i interface. In this case, the photoresponse mechanism can still be described by the processes developed above for type I HIP detectors.

Initial development of Ge BIB detectors by Rockwell scientists (Petroff and Stapelbroek, 1986) led to the development of Si BIBs for LWIR region (15–40 μm). Lately, there has been work on developing GaAs-based BIB detectors (Reichertz *et al.*, 2005; Reichertz *et al.*, 2006; Haller and Beeman, 2002). In GaAs BIB detectors, the low donor-binding energy, giving rise to an impurity transition energy of ∼4.3 meV, is the key for terahertz detection. According to Reichertz *et al.* (2006), detection of terahertz radiation upto ∼300 μm (1 THz) was expected. However, the material quality in the barriers of BIB structures needs to be very high in order to obtain high performance. This has been one of the problems for GaAs BIB detectors, hence, only preliminary results are presently available. Recently, Cardozo *et al.* (2005) has reported high absorption of terahertz radiation near ∼300 μm (1 THz) for a GaAs BIB structure grown by liquid phase epitaxy. Also, the absorption coefficient drops to 50% of the maximum at ∼333 μm (0.9 THz). A list of several terahertz BIB detector details are given in Table 5.1.

TABLE 5.1 Several terahertz BIB detectors along with their performances. Here, f_t is the threshold frequency, λ_t is the threshold wavelength, λ_p is the peak wavelength, η is efficiency, and T is the operating temperature

Reference	Material System	f_t (THz)	λ_t (μm)	λ_p (μm)	η (%)	T (K)
Watson and Huffman (1988)	Ge:Ga	1.6	187	150	4	1.7
Watson *et al.* (1993)	Ge:Ga	1.36	220	150	14	1.7
Bandaru *et al.* (2002)	Ge:Sb	1.5	120	120	—	2
Beeman *et al.* (2007)	Ge IBIB	1.35	222	104	1.2	1.3

2.1.2. Type II HIP detector: $N_c < N_a < N_0$ ($E_v^{p^+} > E_F > E_v^i$)

For doping concentrations above the Mott transition, the impurity band merges with the valence band, and the p^+-layer becomes metallic. However, as long as the concentration does not exceed a critical concentration N_0, the Fermi level can still be above the valence band edge of the *i*-layer ($E_F > E_v^i$) because of the bandgap-narrowing effect. The difference between the Fermi level and the valence band edge in the barrier then forms a workfunction $\Delta_d = E_F - E_v^i$ at the emitter/barrier interface as seen in Fig. 5.2B. The detectors operate by free-carrier absorption, followed by internal photoemission of the excited carriers and sweep out of the emitted carriers by an externally applied electric field. Because the workfunction in theory can be reduced to a small value as desired by adjusting the doping concentration, no restriction on λ_t was expected. However, λ_t was found to be limited by hole transitions (Perera *et al.*, 2003). Although the free-carrier absorption in Type II HIP detectors is less than what is found in Schottky barrier detectors which they resemble, they have a higher internal quantum efficiency as a result of a lower Fermi level and increased hot electron scattering lengths. For heterojunction detectors, the only difference is in the formation of the barrier which has an additional component Δ_x from the band offset because of the material difference, making the total workfunction $\Delta = \Delta_d + \Delta_x$. The basic absorption, photoemission, and collection will be the same as in the homojunction case.

2.1.3. Type III HIP detector: $N_a > N_0$ ($E_F < E_v^i$)

When the doping concentration is so high that the Fermi level is above the conduction band edge of the *i*-layer, the p^+-layer becomes degenerate. The space charge region causes a barrier to form at the $p^+ - i$ interface as a result of the electron diffusion, as shown in Fig. 5.2C. The barrier height depends on the doping concentration and the applied voltage, giving rise to an electrically tunable λ_t. This type of device was first demonstrated by Tohyama *et al.* (1991) using a structure composed of a degenerate n^{++} hot carrier emitter, a depleted barrier layer (lightly doped *p*, *n*, or *i*), and a lightly doped *n*-type hot carrier collector. As the barrier height decreases at higher biases, the spectral response shifts toward the longer wavelength, and the signal increases at a given wavelength. The photoemission mechanism of type III HIP detectors is similar to that of type II HIP detectors, with different response wavelength ranges and different operating temperature ranges resulting from differences in the barrier heights. The type II HIP detector is an FIR detector, and it usually operates at temperatures much lesser than 77 K. In contrast, the type III HIP detectors operate near 77 K and have responses in the MWIR and LWIR ranges (Shepherd, 1992).

2.2. Workfunction dependence on doping concentration above the Mott transition

When the doping concentration is above the metal-insulator transition (Mott transition) concentration value, the detector can be regarded as a metal photoemitter (type II detector). According to the material composition of the two regions of the detectors (i.e., emitter and barrier), the detectors can be further categorized as Homojunction Interfacial Workfunction Internal Photoemission (HIWIP) or HEterojunction Interfacial Workfunction Internal Photoemission (HEIWIP) detectors. The band offset produced by the doping difference alone in HIWIPs is because of the bandgap-narrowing effect, and this offers a detection capability in the FIR region. In contrast, the offset can be controlled by adjusting the bandgap difference between materials forming HEIWIPs. This is also the case of *p*-doped HEIWIPs using the absorption mechanism by hole transitions between inter-valence bands, showing the capability of uncooled operation in the MWIR spectral range as discussed in Section 3.

2.2.1. Barrier height variation in HIWIPs

There are four major contributions to the bandgap narrowing because of doping (Jain *et al.*, 1991): (1) the shift of the majority band edge as a result of the exchange interaction; (2) the shift of the minority band edge because of carrier–carrier interaction or electron–hole interaction; (3) the shift of the majority band edge due to carrier–impurity interactions; (4) the shift of the minority band edge due to carrier–impurity interactions. The majority band denotes the conduction or valence band in *n*- or *p*-doped materials, respectively. With increased doping, the enhanced contributions leads to shifting of the conduction (or valence) band edge downward (or upward) in the bandgap region. At the same time, the impurity band becomes broaden and asymmetrical. At a critical doping level, the conduction (or valence) and impurity bands merge making the semiconductor to behave as a metal (Mott transition). Above the Mott transition, with further increasing the doping concentration, the impurity band starts to shrink and finally becomes absorbed into the conduction band (Jain *et al.*, 1991).

It has been shown (Perera *et al.*, 1995) that raising of the valence band edge ΔE_v (lowering of the conduction band edge, ΔE_c) can be described using the high-density (HD) theory. HD theory (Jain *et al.*, 1991) describes the behavior of heavily doped Si, GaAs and Ge to a fair degree of accuracy in the high-density regimes, i.e., above the Mott critical concentration, and gives reasonable results even at doping concentrations as low as 10^{18} cm^{-3}. The main result of this theory is that the electron–electron interaction (manybody effect) causes a rigid upward (downward) shift of the valence (conduction) band, ΔE^{ex}, which is also known as the exchange energy.

The electron–impurity interaction causes an additional shift, ΔE^i, and also distorts the density of states function. In this theory, the semiconductor is assumed to be uncompensated with completely ionized impurities so that the free carrier concentration is equal to the donor doping concentration N_d. In principle, this theory is valid close to 0 K.

Jain and Roulston (1991) have derived a simple and accurate expression for the shift of the majority band edge, ΔE_{maj}, that can be used for all *n*- and *p*-type semiconductors and for any doping concentration in the high-density regime. By introducing a correction factor to take deviations from the ideal band structure (anisotropy of bands for *n*-type material) into account the workfunction for the homojunction has been obtained (Perera and Shen, 1999).

As seen in Fig. 5.3, as the hole doping concentration N_a increases more than 10^{19} cm^{-3}, λ_t becomes sensitive to N_a; hence, only a small increase in N_a can cause a large increase in λ_t. It should be pointed out that although the high-density theory is valid in the high-doping range ($N_a > N_c$), it can not be used for moderately doped semiconductors where N_a is in the neighborhood of N_c (Jain *et al.*, 1991). The metal-to-nonmetal transition and several properties of moderately doped semiconductors, such as the Fermi level position, the shape of density-of-states which is highly distorted in this case, cannot be modeled by this theory.

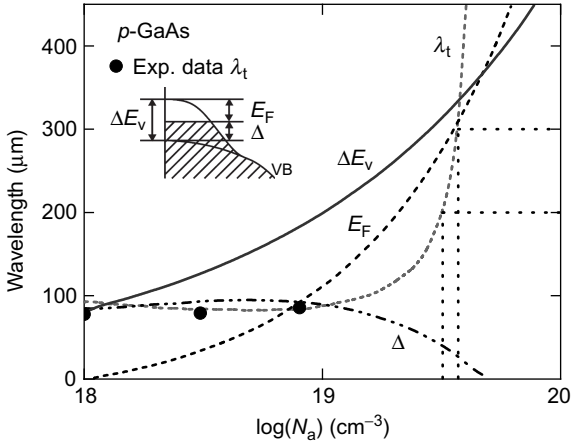

FIGURE 5.3 Doping concentration dependence of ΔE_c (ΔE_v), E_F, Δ, and λ_t, calculated using the high-density theory for p-type GaAs. The experimental λ_t obtained from p-GaAs HIWIP detectors are shown by solid circles. The dotted lines indicate concentration (3.2×10^{19} and 3.6×10^{19} cm^{-3}) needed to obtain $\lambda_t = 200$ and $300\,\mu$m, respectively, at low bias.
Reused with permission from Perera and Shen (1999). Copyright 1999, Springer.

To determine the Δ versus N_a relationship in the intermediate doping range, other theories, such as Klauder's multiple scattering theory (Klauder, 1961), are needed. In theory, the workfunction Δ_d can be varied almost close to zero by controlling the doping concentration giving rise to wavelength tailorable HIWIP detectors.

2.2.2. Barrier height variation in HEIWIPs

HEIWIP detectors which combine the free-carrier absorption of the HIWIP (Homojunction Interfacial Workfunction Internal Photoemission) detectors (Shen *et al.*, 1997) with the material composition of Quantum Well Infrared Photodetectors (QWIPs) have been experimentally demonstrated (Perera *et al.*, 2001), covering the wavelength range from 4 to 124 μm. The typical HEIWIP detector structure consists of a *p*-doped GaAs emitter (absorber) region followed by an undoped AlGaAs barrier region. Although the structure appears similar to that of a *p*-type QWIP, the emitter/absorber in a HEIWIP is thicker than the well of a QWIP. As a result, the carriers form a three-dimensional distribution in HEIWIPs rather than being in quantized states as in a QWIP. The basic idea of HEIWIP detectors is to add the valence band offset for the GaAs/AlGaAs interface to the offset from the doping (N_A) in the emitters. The contribution from the doping (Δ_d) is the same as for HIWIPs. The Al fraction contribution is taken as $\Delta_{Al} = (x * 530)$ meV where x is the Al fraction. The total barrier at the interface is then $\Delta = \Delta_d + \Delta_{Al}$.

λ_t can be determined directly from $\lambda_t = 1.24/\Delta$, where λ_t is in micrometer and the workfunction Δ is in electron volts. A practical lower limit for the Al fraction is around $x \geq 0.005$, which corresponds to $\lambda_t \leq 110\,\mu$m. Further increase in λ_t beyond 110 μm requires a change in the design because the minimum Δ is limited by the bandgap-narrowing Δ_d. One possible approach to avoid this limit is to use AlGaAs as the emitter and GaAs as the barrier (Rinzan *et al.*, 2005b). In such a device, the bandgap narrowing in the doped AlGaAs is partially offset by the increased bandgap of the AlGaAs material relative to the GaAs, giving $\Delta = \Delta_d - \Delta_{Al}$. For example, a $\lambda_t = 335\,\mu$m detector would have an Al fraction of $\sim$0.01. The FIR absorption in AlGaAs is very similar to GaAs (Rinzan *et al.*, 2005a) because of the very-low Al content giving performances similar to the devices with AlGaAs barriers. Another approach is to increase doping concentrations to reduce the bandgap-narrowing contribution. This has been done in *n*-type GaAs/AlGaAs structures (Weerasekara *et al.*, 2007) leading to detectors with response out to 94 μm. The variation of λ_t with the Al fraction for *n*-type AlGaAs HEIWIPs and *p*-type HEIWIPs using both GaAs and AlGaAs emitters is shown in Fig. 5.4. The experimentally observed thresholds are represented by symbols, which will be discussed later.

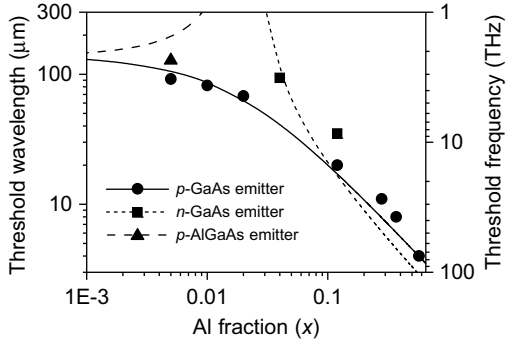

FIGURE 5.4 The variation of the threshold frequency with Al fraction for n-type HEIWIPs using GaAs emitters, and for p-type HEIWIPs with GaAs and AlGaAs emitters. The symbols represent the experimentally observed thresholds, which will be discussed later.

2.3. Theoretical modeling of light propagation in the multi-layer structure

A semiconductor detector structure consists of multiple layers in which the light propagation can be described (Esaev *et al.*, 2004a) using the transfer matrix method (Klein and Furtac, 1986) with each layers modeled by the complex refractive index and complex permittivity (Blakemore *et al.*, 1982). By applying continuity conditions (the electric field and its derivative for transverse electric [TE] waves, or the magnetic field and its derivative for transverse magnetic [TM] waves) across the interfaces, one can deduce the following transfer matrix M connecting the incoming (E_0), reflection (rE_0), and transmission (tE_0) light:

$$\begin{pmatrix} E_0 \\ rE_0 \end{pmatrix} = M \cdot \begin{pmatrix} tE_0 \\ 0 \end{pmatrix} = \begin{pmatrix} M_{11} & M_{12} \\ M_{21} & M_{22} \end{pmatrix} \cdot \begin{pmatrix} tE_0 \\ 0 \end{pmatrix}, \tag{5.1}$$

where E_0 denotes the electric field. The reflection r and transmission t coefficients are calculated by

$$r = M_{21}/M_{11}; \quad t = 1/M_{11}. \tag{5.2}$$

The reflectance $\mathcal{R}$ and transmittance $\mathcal{T}$ of the complete structure were defined as $\mathcal{R} = |r|^2$ and $\mathcal{T} = (n_{\text{out}}/n_{\text{in}})|t|^2$ (for TE) or $\mathcal{T} = (n_{\text{in}}/n_{\text{out}})|t|^2$ (for TM), where n_{in} and n_{out} are the real component of refractive index of the media for light incoming and outgoing, respectively. Total absorption in the structure was calculated as the difference between unity and the sum of the reflectance and transmittance $\mathcal{A} = 1 - \mathcal{T} - \mathcal{R}$.

The depth to which the incident radiation penetrates into the layers, skin depth $\delta(\lambda)$, depends on the wavelength, doping concentration N, and

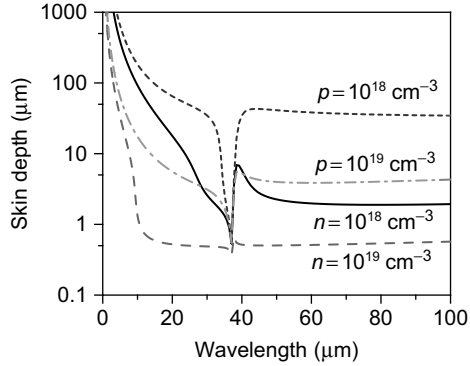

FIGURE 5.5 Skin depth for infrared radiation in GaAs with both n- and p-type doping of 10^{18} and 10^{19} cm^{-3}. The skin depth is relatively constant at long wavelength and increases rapidly at short wavelength. The feature between 8.5 and 7.5 THz (35 and 40 μm) is because of the reststrahlen effect. Skin depth is least for n-type material. Reused with permission from D. G. Esaev, Journal of Applied Physics, 96, 4588 (2004). Copyright 2004, American Institute of Physics.

effective mass of the free carriers. The variations of $\delta(\lambda)$ with wavelength for an n- and p-type GaAs layers with doping concentrations 10^{18} and 10^{19} cm^{-3} have been calculated (Esaev *et al.*, 2004a) and are shown in Fig. 5.5. At shorter wavelength, $\delta(\lambda)$ is high and has a strong wavelength dependence, whereas at higher wavelength $\delta(\lambda)$ approaches a plateau. Hence, a thin emitter layer will be almost transparent to lower wavelength, providing a negligible contribution to the photocurrent.

It is suggested that because of the shorter skin depth of n-type layers at the same doping concentration causing higher reflectivity than p-type, n-type layers are better for mirrors inside the structure, allowing selective increase of absorption of photons at desired wavelength (Esaev *et al.*, 2004a), leading to enhanced detector response. A model for optimizing the response has been suggested (Zhang *et al.*, 2002), with experimental confirmation of enhanced absorption in a device structure (Zhang *et al.*, 2003).

2.4. Responsivity

The responsivity of a photodetector at wavelength λ is given by (Esaev *et al.*, 2004a)

$$R = \eta g_{\mathrm{p}} \frac{q}{hc} \lambda, \tag{5.3}$$

where h is Planck's constant, η is total quantum efficiency, and g_{p} is the photoconductive gain. The responsivity calculations included effects

of photoexcitation of carriers in the emitter, hot carrier transport, thermalization, and photoemission into the barrier. Total quantum efficiency (Perera *et al.*, 1995), which is the product of photon absorption η_a, internal photoemission η_i, and hot-carrier transport probabilities is given as η_t, $\eta = \eta_a \eta_i \eta_t$. The η_i, was described by an "escape cone" model (Williams, 1970), and η_t followed the Vickers–Mooney model (Vickers, 1971; Mooney and Silverman, 1985).

The absorption probability is proportional to the imaginary part of the permittivity. In determining the absorption for use in responsivity, only the photoexcitation is included, and not the contributions from phonon generation. Radiation absorbed through optical phonon generation is dissipated in the crystal lattice, without producing any hot carriers, and hence does not contribute to the photocurrent. The absorption coefficient is related to the skin depth as $\alpha(\lambda) = 2/\delta(\lambda)$. As shown in Fig. 5.5, $\delta(\lambda)$ for n-type GaAs is about 10 times lower than for p-type at doping concentrations of 10^{19} cm^{-3} for wavelengths longer than 8 μm. This increased absorption is because of the reduced carrier mass of the electrons compared with the holes. Details of the responsivity calculations can be found in the study of Esaev *et al.* (2004a).

2.5. Dark and noise current

The dark current of a detector plays a major role in the device performance. Dark current variation with temperature allow the determination of the workfunction through Arrhenius plots (Sze, 1981). Dark current in the HEIWIP structure is a sum of the thermo-emission current over the barrier and the tunneling current through the barrier (Perera *et al.*, 1995). The thermionic current in the HEIWIP structure can be described in the frame of the 3D carrier drift model (Kane *et al.*, 1992). The measured and calculated dark currents and the 300 K photocurrent for a HEIWIP detector with a λ_t of 124 μm at various temperatures are shown in Fig. 5.6.

As FIR detectors typically operate at low temperatures, the thermal noise is typically negligible in these detectors. Hence, the primary sources of noise in the devices are the shot noise from the injection of carriers into the detector at the contact barrier interface, and the generation–recombination (g–r) noise from the carrier capture and emission from trap states. In most cases, the shot noise will dominate the g–r noise at high frequencies and the noise current is related (Levine, 1993) to the mean current through the detector, $\bar{I}$ by:

$$I_{\text{noise}}^2 = 4q\bar{I}g_n\Delta f \tag{5.4}$$

where g_n is the noise gain and δf is the measurement bandwidth.

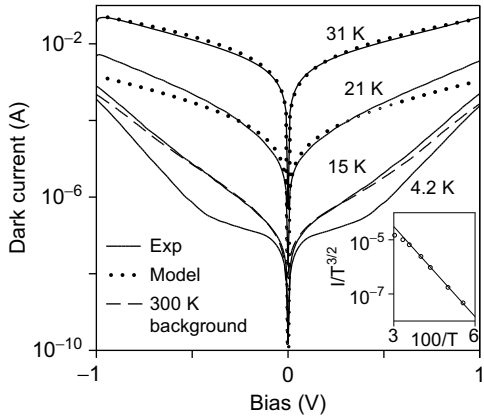

FIGURE 5.6 Dark current at various temperatures for the HEIWIP detector. The dark current at 10 K is almost the same as for 4.2 K. Also shown is the 300 K background current (dashed line) indicating BLIP operation at 14 K.
Reused with permission from Perera *et al*. (2001). Copyright 2001, American Institute of Physics.

The noise gain g_n and photocurrent gain g_p are given by (Ershov and Liu, 1999)

$$g_n = \frac{1 - p_{c/2}}{p_c(N+1)} + \frac{1 - (1-p_c)^{N+1}}{p_c(N+1)^2[1-(1-p_c)^N]} \tag{5.5}$$

$$g_p = \frac{1}{p_c N} \tag{5.6}$$

where p_c is the capture probability of a carrier traversing an emitter, and N is the number of such emitters. The ratio g_n/g_p varies from 0.5 to 1 when p_c varies from 0 to 1 and N from 1 to infinity. Hence, the difference between them may be ignored in many applications, particularly if the capture probability is low.

Typical noise current spectra (Perera and Shen, 1999) of a p-GaAs HIWIP FIR detector at 4.2 K for various forward bias values are presented in Fig. 5.7. Similar noise behavior was observed under reverse bias conditions. All the spectra display $1/f$ noise dependence at frequencies (f) less than 1 kHz and are independent of frequency at higher values.

The $1/f$ noise power density is proportional to I_d^α with an α value of $2.05 \sim 2.10$. This type of behavior indicates that the origin of the $1/f$ noise could be interpreted in terms of a random fluctuation in the occupancy of the interface trap centers that can lead to generation–recombination (g–r)

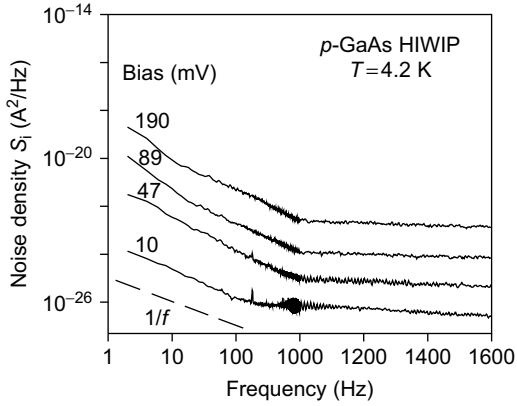

FIGURE 5.7 Measured dark current noise spectra of p-GaAs HIWIP far-infrared detector at 4.2 K for various forward biases. The dashed line represents the $1/f$ dependence of the noise power density S_i.
Reused with permission from Perera and Shen. (1999). Copyright 1999, Optical Society of America.

$1/f$ noise (Jantsch, 1987). Two representative models of the $1/f$ noise have been proposed (Shklovskii, 1980; Luo *et al.*, 1988).

The noise measurements could also be used for gain determination (Levine, 1993). For frequencies above 1 kHz, the noise was independent of frequency and was dominated by shot noise. The determined gain increases rapidly with bias at low voltages and then saturates (Perera and Shen, 1999). This behavior is similar to the case of QWIPs (Levine, 1993). The highest value of g recorded for this detector was $\sim$0.95 (Perera and Shen, 1999) at a bias corresponding to the highest responsivity, in good agreement with the estimation of 0.984, by combining the experimental responsivity and quantum efficiency.

2.6. Homojunction detectors

HIWIP detectors have been demonstrated based on different material systems. In general, the doping in the emitter of HIWIP detectors is higher than that of HEIWIP detectors. While p^+-Si/Si HIWIPs were developed (Perera *et al.*, 1998) some times ago, p^+-GaAs/GaAs HIWIPs were started to be developed because of the rapid development and growth of GaAs. Presently, HIWIPs based on other materials, such as GaSb (Jayaweera *et al.*, 2007), have also been tested; however, the progress of growth techniques plays a role for these new materials to be used for potential high-performance detectors. In HIWIPs, the active region consists of a

TABLE 5.2 A comparison of different HIWIP detectors. Here, f_t is the threshold frequency, λ_t is the threshold wavelength, R_P is the peak responsivity, λ_P is the peak wavelength, and D^* is the detectivity

Reference	Material System	f_t (THz)	λ_t (μm)	R_P (A/W) at λ_P	T (K)	D^* (Jones)
Perera *et al.* (1998)	p^+-Si/Si	6.25	48	12.3 at 28	4.2	6.6×10^{10}
Ariyawansa *et al.* (2006b)	p^+-Si/Si	8.6	35	1.8 at 25	4.6	1.2×10^{11}
Jayaweera *et al.* (2007)	p^+-GaSb/GaSb	3.1	97	31 at36	4.9	5.7×10^{11}
Shen *et al.* (1997)	p^+-GaAs/GaAs	3.0	100	3.1 at 34	4.2	5.9×10^{10}
Esaev *et al.* (2004b)	p^+-GaAs/GaAs	4.3	70	7.4 at 34	4.2	3.6×10^{11}

junction formed by a doped layer (emitter) and undoped layer (barrier) made of the same material. The primary detection mechanism in a HIWIP involves free-carrier absorption, internal photoemission across the barrier, and the carrier collection. The interfacial workfunction (Δ), which arises because of doping different in the emitter and the barrier, determines the terahertz threshold. Several HIWIPs are listed in Table 5.2.

2.6.1. p^+-Si/Si HIWIP detectors

Si *p-i-n* diodes under forward bias has shown various infrared response thresholds from MWIR to FIR. A device (Perera *et al.*, 1992, 1993) with a peak responsivity of 1.5×10^4 V/W at 30 μm showed a threshold of 57 μm, while another Si *p-i-n* diode (Perera *et al.*, 1992) showed a response up to 220 μm at 1.5 K. Following this, a Silicon *p*-type HIWIP sample was specifically developed for FIR detection (Perera *et al.*, 1998). The spectral response at 4.2 K measured at different forward biases and having a wide spectrum with high responsivity is shown in Fig. 5.8. The tailing behavior at short wavelengths reflects the nature of internal photoemission. The responsivity has a similar spectral shape and strong bias dependence for both polarities, increasing significantly with increasing bias. However, the bias cannot increase indefinitely as the dark current also increases with bias.

Several sharp peaks were seen in the spectra under high biases, becoming stronger with increasing bias. At low biases, the photoconductivity is because of the usual photon capture by the impurity states, where λ_t of the response is determined by the energy gap Δ. At high biases, for high-enough doping concentration, the wave functions of excited impurity states overlap, leading to hopping conduction among ionized dopant sites. These peak positions are in good agreement with the theoretical energies of transitions from the ground states to the first ($2P_0$), second ($3P_0$), and third ($4P_0$) excited states (marked by arrows in Fig. 5.8; Perera *et al.*, 1998). For this device, the λ_t was reported (Perera *et al.*, 1993) as 50 μm at low biases, decreasing to around 90 μm at a bias of 0.79 V. The highest

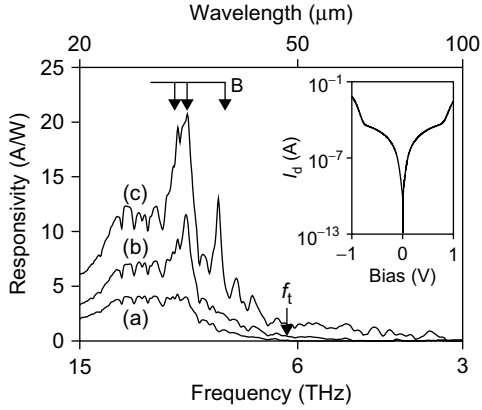

FIGURE 5.8 Spectral response of p-Si HIWIP FIR detector measured at 4.2 K under different forward (top positive) bias V_b (a) 0.377V, (b) 0.539V, and (c) 0.791V. A peak responsivity of 12.3 A/W is observed at 10.9 THz (27.5 μm) in curve (c). The sharp response peaks are associated with excited impurity states with the theoretical energy levels marked by arrows. The other minor features are because of the instrument response function against which the detector output was rationed. The inset shows the variation of the dark current, I_d, with bias at 4.2 K.
Reused with permission from Perera *et al.* (1998). Copyright 1998, American Institute of Physics.

responsivity reported was 12.3 ± 0.1 A/W at 27.5 μm and 20.8 ± 0.1 A/W at 31 μm. Hopping conduction can be clearly seen in the I–V data in the inset of Fig. 5.8, where the dark current increases rapidly with bias more than 0.75 V. The highest D^* (6.6×10^{10} Jones for 4.2 K under a bias of 10 mV at 27.5 μm) occurred at low biases because the dark current increases rapidly with the bias. However, D^* also increases slightly with the bias because of the rapid increase in responsivity, and finally decreases again because of the onset of hopping conduction.

2.6.2. p^+-GaSb/GaSb HIWIP detectors

A p^+-GaSb/GaSb HIWIP detector structure responding up to 97 μm has also been reported (Jayaweera *et al.*, 2007). In a separate publication (Perera *et al.*, 2008), it has been reported that a similar GaSb-based HIWIP detector also responds with a flat response in the terahertz range (100–200 μm) as shown in Fig. 5.9. The sharp dip at ~43 μm is because of reststrahlen absorption in GaSb. Based on the Arrhenius calculation, the activation energy was reported as 128 meV, which is in good agreement with the observed free carrier threshold of 97 μm. The flat response in the range 100–200 μm is relatively weak compared with the free carrier response, but

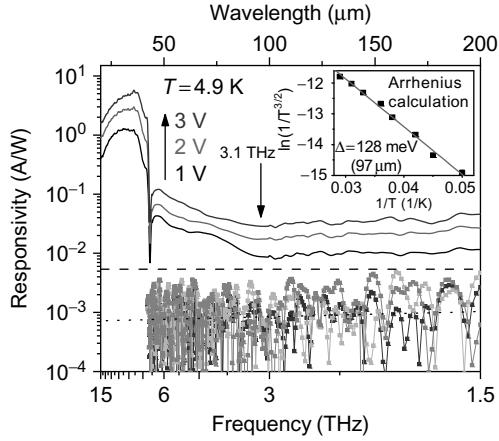

FIGURE 5.9 The response of a p^+-GaSb/GaSb HIWIP detector in the 15–1.5 THz range at 1, 2, and 3 V bias voltages at 4.9 K. The arrow indicates the free-carrier response wavelength threshold at the 3.1 THz (97 μm). The noise curves at the bottom were obtained under dark conditions, and the dashed line shows the maximum noise level of the spectral response measurement setup. The Arrhenius curve, which translates to an activation energy of 128 meV (97 μm) is also shown in the inset.
Reused with permission from Perera *et al*. (2008). Copyright 2008, Elsevier.

is an order of magnitude higher than the system noise level as shown in Fig. 5.9. Although the mechanism of this response has also not been established yet as in the case of terahertz response in GaN/AlGaN structure, this result also implies the possibility of developing GaSb/InGaSb terahertz HEIWIP detectors, which would provide flexibility in controlling the threshold with the In fraction. Based on the lower band gap offset between GaSb and InSb, it is clear that λ_t of 300 μm could be achieved, while keeping the In fraction in the practical range. Therefore, GaSb-based HEIWIPs would also be possible substitutions for GaAs, where high accuracy of the alloy fraction (Al fraction in AlGaAs) is needed to control the threshold.

2.6.3. p^+-GaAs/GaAs HIWIP detectors

The spectral responses reported at different forward biases for a GaAs HIWIP sample consisting of 20 periods of 4×10^{18} cm^{-3} doped GaAs emitters and undoped GaAs barriers are shown in Fig. 5.10. This was the highest response as well as the longest λ_t (100 μm) reported for GaAs HIWIP detectors (Shen *et al.*, 1997). The long tailing behavior in the long wavelength region reflects the nature of internal photoemission. This detector reported a peak response of 3.1 A/W for a bias of 192 mV, and

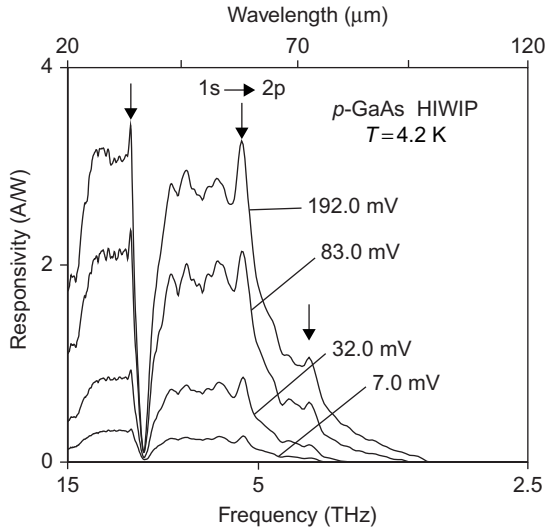

FIGURE 5.10 Spectral response measured at 4.2 K for a p-GaAs HIWIP detector with emitters doped to $8 \times 10^{18}\,\mathrm{cm}^{-3}$ at different forward biases.
Reused with permission from Shen *et al*. (1997). Copyright 1997, American Institute of Physics.

the peak D^* was 5.9×10^{10} Jones for a bias of 83 mV at 4.2 K and 34 μm (Esaev *et al*., 2004b).

2.7. Light–heavy hole transition effects

Although, in principle, the barrier height can be reduced to any desired value by increasing the doping in the emitter, it was reported (Perera *et al*., 2003) that the transitions between the light and heavy hole states in detectors lead to a decrease in the expected λ_t. The measured and calculated values (Δ and λ_t) from HD theory as well as the values predicted from the light-heavy hole transitions are shown in Fig. 5.11. This calculation (Shen *et al*., 1998) used a modified Fermi level expression, which provides a correction for the difference in the values for the Fermi level determined by the conventional density of state calculation and the values determined by the experimental luminescence spectra (Jain and Roulston, 1991). From this correction, the effect on the workfunction was $\sim 5 \pm 1$ meV, as can be observed from a comparison between the curves in Figs. 5.3 and 5.11. The reported values of Δ were obtained using Arrhenius plots of the current versus temperature, whereas λ_t was obtained from the spectral measurements. For low-doping densities ($<10^{19}\ \mathrm{cm}^{-3}$), the predicted values of both

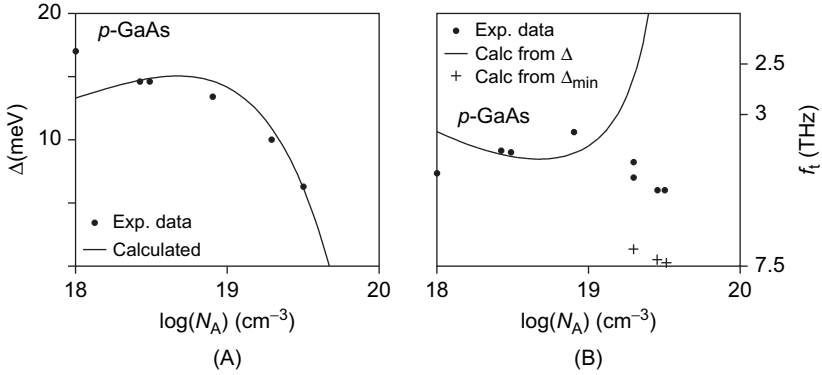

FIGURE 5.11 Plots of (A) calculated and measured (based on from Arrhenius analysis) workfunction Δ and (B) calculated and measured (from response spectra) f_t versus doping in HIWIP detectors. The solid line indicates the results from the HD theory while the points (•) are the experimental results. Also shown in (B) are the threshold limit (+) calculated from the heavy–light hole transition.
Reused with permission from Perera *et al.* (2003). Copyright 2003, Elsevier.

quantities were in good agreement with the measured values. However, at higher doping where λ_t was expected to increase, it remained nearly constant even though the measured Δ decreased as expected. The differences between spectral and Arrhenius results were explained (Perera *et al.*, 2003) in terms of direct excitations from the heavy-to-light hole bands. For highly doped materials, the carriers excited directly into the light hole band can escape leading to reduced population in the heavy hole band, and hence a reduced λ_t. This is the reported cause for the limit on the effective threshold for *p*-type detectors even at high doping (Perera *et al.*, 2003).

2.8. Heterojunction detectors

In HIWIP detectors, the only way to adjust λ_t is through the doping concentration, which encounters difficulties in controlling the barrier height and extending the threshold to longer wavelength (Perera *et al.*, 2003). This difficulty has led to the development of the HEIWIP detectors (Perera and Matsik, 2007) which use the Al fraction in one or both of the layers as an additional degree to tailor λ_t. The band diagram for two different types of *p*-doped HEIWIP detectors using GaAs and AlGaAs are shown in Fig. 5.12. The choice between these two types of detectors is determined by desired λ_t. The first type (Fig. 5.12A) is the standard HEIWIP detector, which uses doped GaAs emitters and undoped AlGaAs barriers. The contributions

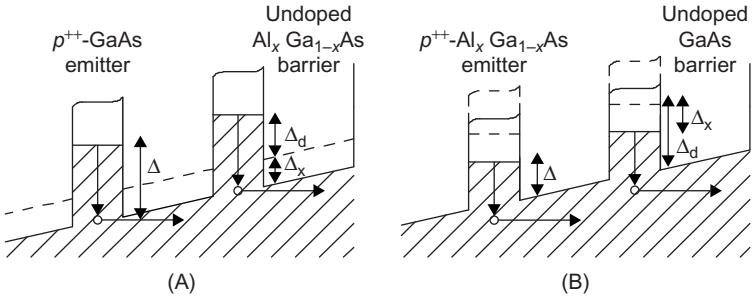

FIGURE 5.12 (A) The band diagram for a HEIWIP detector using doped GaAs emitters and undoped AlGaAs barriers. The contributions from both the doping and the Al fraction will increase the workfunction. (B) The band diagram for a HEIWIP detector using doped AlGaAs emitters and undoped GaAs barriers. Here the contribution from doping increases the workfunction while the contribution from the Al fraction decreases it.

from the doping and Al fraction to the workfunction are both in the same direction, i.e., reducing the Al fraction can increase λ_t from a minimum of $\sim$2 μm for an AlAs emitter up to a limit of $\sim$110 μm for an Al fraction of 0.005. The upper limit is due to the Al fraction at which the Al starts to act as an isoelectronic dopant and does not produce a consistent change in the valence band. Although an Al fraction of zero is possible, that would correspond to the HIWIP case which had a limitation in λ_t. The second type of design uses doped AlGaAs as the emitter, and undoped GaAs as the barrier as shown in Fig. 5.12B. In this approach, the band offset from the Al fraction is used to reduce the band offset from the doping in the emitter. In this approach, the Al fraction must be kept small ($x < 0.17$) such that the band offset does not exceed the doping offset. In theory, this approach will allow the workfunction to be reduced down to zero. Several HEWIPs are listed in Table 5.3.

2.8.1. *p*-GaAs emitter/AlGaAs barrier HEIWIP detectors

Results were reported (Perera *et al.*, 2001) on a device structure consisting of 20 periods of 158 Å GaAs wells and 800 Å $Al_{0.02}Ga_{0.98}As$ barriers. The wells were doped with Be to 3×10^{18} cm^{-3}. The response increased as the bias was increased up to $\sim$200 mV after which it remained relatively constant. Strong response was reported for wavelength less than 50 μm with a λ_t of 70 μm. The peak responsivity was $\sim$6 A/W at a wavelength of 32.5 μm. The specific detectivity (D^*) was $\sim 2 \times 10^{13}$ cm$\sqrt{\text{Hz}}$/W (Jones), with a Noise Equivalent Power (NEP) of 1.4×10^{-15} W/$\sqrt{\text{Hz}}$ (Perera *et al.*, 2001).

TABLE 5.3 A comparison of different HEIWIP detectors. Here, f_t is the threshold frequency, λ_t is the threshold wavelength, R_P is the peak responsivity, λ_P is the peak wavelength, and D^* is the detectivity

Reference	Material System	f_t (THz)	λ_t (μm)	R_P (A/W) at λ_t(μm)	T (K)	D^* (Jones)
Perera *et al.* (2001)	p^+-GaAs/ $Al_{0.02}Ga_{0.98}As$	4.3	70	6 at 32.5	4.2	2×10^{13}
Matsik *et al.* (2003)	p^+-GaAs/ $Al_{0.01}Ga_{0.99}As$	3.6	84	5.4 at 30.7	4.2	4×10^{10}
Matsik *et al.* (2003)	p^+-GaAs/ $Al_{0.005}Ga_{0.995}As$	3.3	92	5.9 at 30.7	4.2	3.6×10^{10}
Rinzan *et al.* (2005b)	p^+-$Al_{0.005}Ga_{0.995}As$/ GaAs	2.3	130	7.3 at 31	4.8	5.3×10^{11}
Weerasekara *et al.* (2007)	n^+-GaAs/ $Al_{0.04}Ga_{0.96}$	3.2	93	6.5 at 42	6	5.5×10^{8}

Device structures with different Al fractions from 0.005 to 0.02 showing variations in the threshold from 92 to 68 μm have been reported (Matsik *et al.*, 2003). The Al fraction was varied, with x = 0.02, 0.01, and 0.005, respectively, to adjust λ_t, with the expected barrier heights of 18, 13.5, and 11.2 meV, respectively. The responsivity results for the three samples at a bias field of 3.5 kV/cm for 4.2 K are shown in Fig. 5.13 with a strong response for wavelengths less than 50 μm. The inset shows the raw response normalized so that the response was 1 at the wavelength where the signal equaled the noise determined from the deviation of multiple measurements. The threshold values (indicated by the arrows) were $\lambda_t = 65$, 84, and 92 μm for samples with $x = 0.02$, 0.01, and 0.005, respectively. The responsivity at 30 μm was ~5.6 A/W for samples with $x = 0.02$ and 0.01, and 6.0 A/W for $x = 0.005$. The quantum efficiency was 22% for $x = 0.02$ and 0.01, and 25% for $x = 0.005$ at 30 μm. The D^* was 4×10^{10} Jones (cm $\sqrt{\text{Hz}}$/W) for $x = 0.02$ and 0.01 and 3.6×10^{10} Jones for $x = 0.005$ at 4.2 K (Matsik *et al.*, 2003). The variation of λ_t with the Al fraction for p-GaAs/$Al_xGa_{1-x}As$ detectors is summarized in Fig. 5.14. The experimental data from detectors using inter-valence band transitions is also included, which will be discussed in Section 3.

2.8.2. p-AlGaAs emitter/GaAs barrier HEIWIP detectors

As discussed earlier, p-type HEIWIP detectors with GaAs emitters have a λ_t limit because of the limit on Al fraction. One approach to overcome this difficulty is to use AlGaAs emitters with a low aluminum fraction. Absorption measurements have been performed on doped AlGaAs films giving good agreement with the model for the absorption coefficient (Rinzan *et al.*, 2004) as seen in Fig. 5.15A. The model was the same as for the GaAs absorption with the material parameters obtained by a linear interpolation

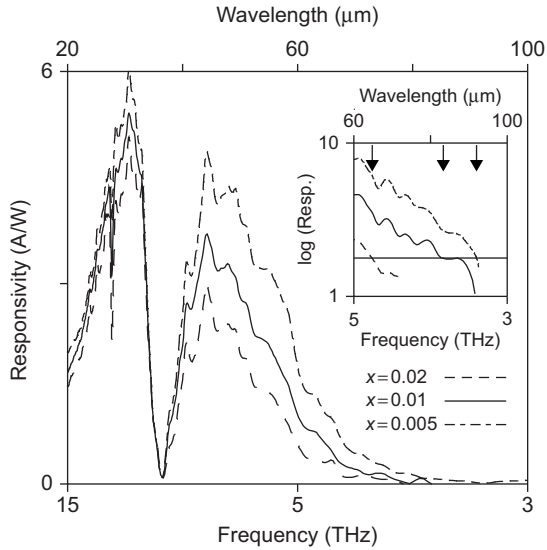

FIGURE 5.13 Experimental responsivity spectra for p-GaAs emitter/$Al_xGa_{1-x}As$ barrier HEIWIP detectors at 3.5 kV/cm obtained at 4.2 K. The only difference in the samples was the Al fraction which was $x = 0.02$, 0.01, and 0.005, respectively. The data shows an increase in λ_t with decreasing x. The sharp decrease near 8 THz is because of the reststrahlen effect. The inset shows a log plot of the raw response with all curves normalized to have the same noise level indicated by the horizontal line. The threshold (indicated by the arrows) variation, with $\lambda_t = 65$, 84, and 92 μm for samples with $x = 0.02$, 0.01, and 0.005, respectively, can be clearly seen.
Reused with permission from Matsik *et al.* (2003). Copyright 2003, American Institute of Physics.

of the values for GaAs and AlAs. Based on these results, detectors using AlGaAs emitters were designed and results have been reported (Rinzan *et al.*, 2005b) on a sample consisting of 10 periods of 3×10^{18} cm^{-3} Be-doped 500- Å thick $Al_{0.005}Ga_{0.995}As$ emitters and 2000-Å thick GaAs barriers sandwiched between two contacts.

The variation of Δ obtained from Arrhenius plots with the bias field for three devices with different electrical areas are shown in Fig. 5.15B. The Δ decreased from ~17 meV at zero bias to 10.5 meV at 2 kV/cm (Rinzan *et al.*, 2005b). The source of this decrease is yet to be explained. The variation of responsivity with the bias field at 4.8 K is shown in Fig. 5.16. For wavelengths <50 μm, the responsivity increases with the field with a maximum responsivity of 9 A/W at 1.5 kV/cm. Although further increase in the field increases the shorter wavelength response, the longer wavelength (>50 μm) response increases as well. As expected, Δ decreases with the field, increasing the threshold to 130 μm for a bias field of 2.0 kV/cm.

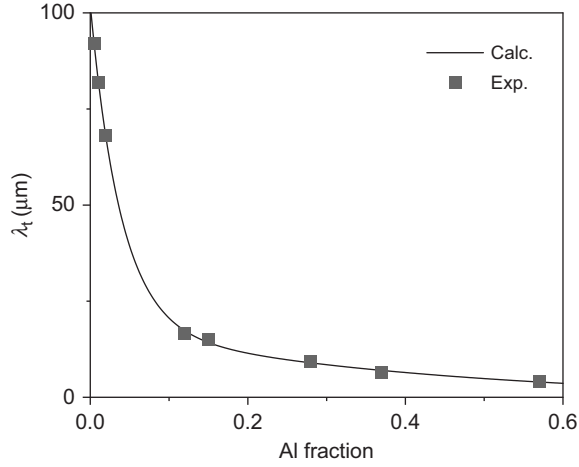

FIGURE 5.14 The variation of λ_t in p-GaAs/$Al_xGa_{1-x}As$ heterojunction detectors. The solid square represents the experimentally observed thresholds in which the data from detectors using inter-valence band transitions as discussed in Section 3 is also included.

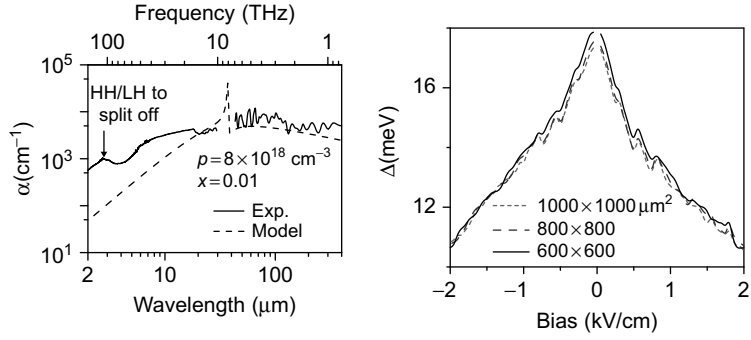

FIGURE 5.15 (A) The measured and calculated absorption coefficient for an $Al_{0.01}Ga_{0.99}As$ film with doping of 8×10^{18} cm^{-3}. For low Al fractions, the experimental results are in good agreement with the model developed for absorption in GaAs. Reused with permission from Rinzan *et al.* (2004). Copyright 2004, American Institute of Physics. (B) Variation of workfunction, Δ with the bias field for three mesas with different electrical areas. The workfunction at different bias fields were obtained using Arrhenius plots. The zero bias workfunction is ~17 meV for all the mesas.
Reused with permission from Rinzan *et al.* (2005). Copyright 2005, American Institute of Physics.

The semilog scale of Fig. 5.16 clearly shows the variation of λ_t with the applied field. A dark current limited peak detectivity of 1.5×10^{13} Jones was obtained at the bias field of 1.5 kV/cm at 4.2 K. A BLIP temperature of 20 K for a 0.15 kV/cm bias field was recorded (Rinzan *et al.*, 2005b).

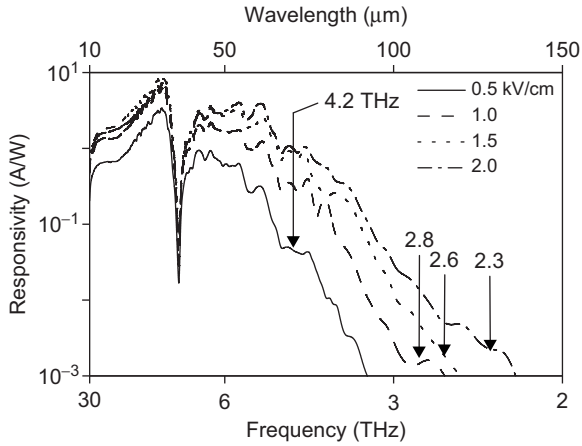

FIGURE 5.16 The variation of responsivity with applied field for p-AlGaAs/GaAs HEIWIP (sample V0207) at 4.8 K. The peak responsivity, 9 A/W at 31 μm was obtained at 1.5 kV/cm. The increase in response with the field around λ_t is because of threshold shift with the bias. The sharp dip at ~37.5 μm is because of the interaction of radiation with GaAs-like TO phonons. The bias field decreases the effective workfunction pushing λ_t toward 150 μm with the increasing field.
Reused with permission from Rinzan *et al*. (2005). Copyright 2005, American Institute of Physics.

2.8.3. n-GaAs emitter/AlGaAs barrier HEIWIP detectors

Most of the HIWIP and HEIWIP work has been carried out based on p-type materials. However, results have been recently reported (Weerasekara *et al.*, 2007) on an n-type GaAs/AlGaAs HEIWIP device structure consisting of an undoped 1-μm thick $Al_xGa_{1-x}As$ ($x = 0.04$) barrier layer sandwiched between two 1×10^{18} cm^{-3} Si-doped GaAs contact layers. The 100-nm top contact and a 700-nm bottom contact layers serve as emitters in this design. The Δ was estimated to be 13–14 meV corresponding to a λ_t of 88–97 μm from Arrhenius analysis (Weerasekara *et al.*, 2007). The calculated Δ should be between ~10–20 meV, corresponding to a λ_t of 60–125 μm.

The maximum peak response (R_{peak}) of 6.5 A/W at 42 μm (Weerasekara *et al.*, 2007) was seen at a bias field of 0.7 kV/cm in the forward bias operation (top emitter positive) as shown in Fig. 5.17A. The R_{peak} obtained in the reversed bias was 1.7 A/W at 0.25 kV/cm. At a bias field of 0.5 kV/cm, The R_{peak} in the forward bias was 6.1 A/W while the R_{peak} in reverse bias is 1.1 A/W. The responsivity ratio in forward and reverse bias operations agrees with the thickness ratio of the bottom and the top contact layers (Weerasekara *et al.*, 2007). Based on the spectral response, a threshold of 94 μm was observed. The variation of

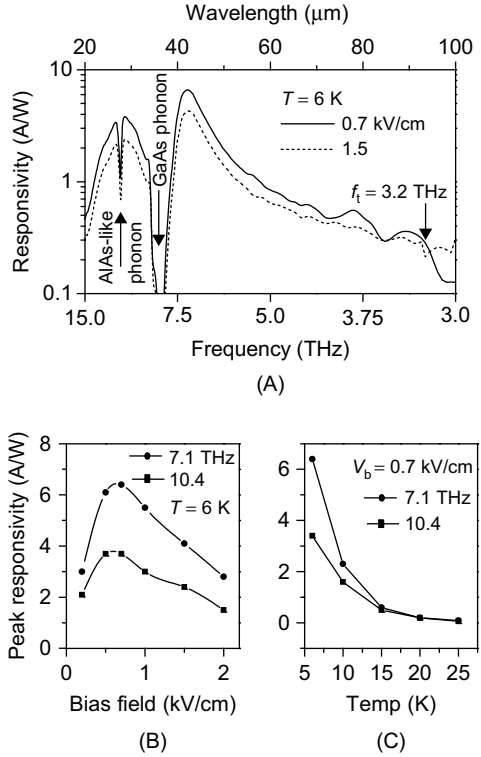

FIGURE 5.17 Responsivity variation of the n-GaAs/AlGaAs HEIWIP for 0.7 and 1.5 kV/cm is shown. The highest R_{peak} is 6.5 A/W at 0.7 kV/cm at 6 K. The λ_t is 94 μm. The λ_t which is 94 μm was determined by the instrument noise level. The inset shows the device structure. Top and Bottom contacts are 100- and 700-nm thick n-doped GaAs, respectively. The barrier is 1-μm thick undoped GaAs/$Al_{0.04}Ga_{0.96}As$. (B) Variation of R_{peak}s at 7.1 and 10.4 THz under different bias fields. (C) The R_{peak} variation with temperature at the bias field of 0.7 kV/cm and responsivity vanishes after 25 K. Reused with permission from A. Weerasekara, Optics Letters 32, 1335 (2007), Copyright 2007, Optical Society of America.

the responsivity values at 29 and 42 μm (10.4 and 7.1 THz) with bias are shown in Fig. 5.17B. The R_{peak} under 0.7 kV/cm bias field decreases from 6.5 to 0.1 A/W, when the operating temperature increases from 6 to 25 K. The variation of the responsivity values at 29 and 42 μm (10.4 and 7.1 THz) with operating temperature is shown in Fig. 5.17C.

The experimentally observed (symbols) and the calculated (lines) thresholds for p-GaAs/AlGaAs, p-AlGaAs/GaAs, and n-GaAs/AlGaAs HEIWIP detectors with different Al fractions are shown in Fig. 5.4. The results for p-GaAs/AlGaAs HEIWIP detectors are based on samples

with $x = 0.02$, 0.01, 0.005; the p-GaAs/$Al_{0.12}Ga_{0.88}As$ HEIWIP detector reported by Matsik *et al.* (2004); and p-GaAs/$Al_xGa_{1-x}As$ HEIWIP detectors ($x = 0.28$, 0.37, and 0.57) reported by Jayaweera *et al.* (2008). The p-$Al_{0.005}Ga_{0.995}As$/GaAs detector reported by Rinzan *et al.* (2004) has shown the highest wavelength threshold. Experimental thresholds of most of the p-GaAs/AlGaAs detectors agree with the calculated values. As seen in the plot corresponding to n-GaAs emitter, the threshold of the n-GaAs/$Al_{0.04}Ga_{0.96}As$ HEIWIP detector reported by Weerasekara *et al.* (2007) is also in good agreement with the theoretical calculation. However, the threshold obtained for an n-GaAs/$Al_{0.12}Ga_{0.88}As$ HEIWIP detector deviates from the calculated value. In any of the detectors considered for the comparison in Fig. 5.4, the actual Al fraction after the growth of the structure in AlGaAs has not been reported, instead the designed Al fraction has been considered for the plot. Because a deviation in the Al fraction during the growth can occur, one of the possible reasons for the slight deviation in the threshold could be because of this difference.

2.8.4. n-GaN/AlGaN HEIWIP detectors

A GaN/AlGaN HEIWIP detector structure responding in the FIR range has also been reported (Ariyawansa *et al.*, 2006c), indicating the feasibility of terahertz detector development with the rapidly developing GaN/AlGaN material system. The detector structure was grown by organo-metallic chemical vapor deposition (OMCVD, same as MOCVD) on a sapphire substrate. The complete response of this detector at 5.3 K is shown in Fig. 5.18 with the response composed of three parts based on three detection mechanisms. The free carrier response exhibits a threshold at 11 μm, while the sharp peak at 54 μm is due to the 1s–$2p_{\pm}$ transition of silicon (Si)-dopant atoms, which has been observed previously (Moore *et al.*, 1997) with the same energy of ∼23 meV. In addition to the free-carrier and impurity-related responses discussed, there is also a slower mechanism which responds out to 300 μm. This response was reported to be due to either a thermal or pyroelectric effect; however, the exact mechanism has not been confirmed yet. Further studies on the response mechanism will benefit the development of GaN-based terahertz detectors.

2.9. Dualband detectors

In both HIWIP and HEIWIP detectors, it has been reported (Ariyawansa *et al.*, 2005) that interband transitions in the undoped barrier and intraband transitions within the emitter lead to dualband response characteristics. Incident radiation with an energy greater than the band gap of the barrier are absorbed, generating an electron–hole pair. The standard detection

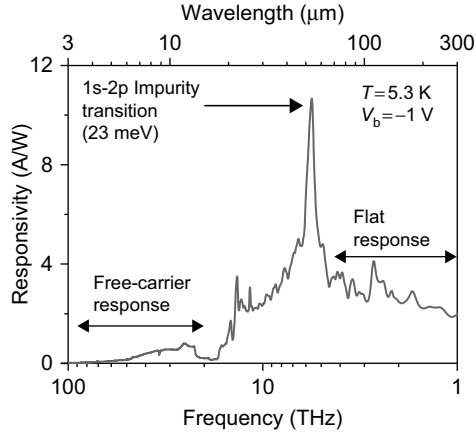

FIGURE 5.18 The response of the GaN/AlGaN HEIWIP detector at 5.3 K and −1 V bias. There are three response mechanisms, which can contribute to the photocurrent: free-carrier response, impurity-related response, and a flat terahertz response.

mechanism in HIWIPs and HEIWIPs including free-carrier absorption leads to the detection of terahertz radiation. Excited carriers are then collected by the applied electric field. The interband response threshold is determined by the band gap of the barrier material. Hence, using different material systems (such as Si, GaAs/AlGaAs, GaN/AlGaN, and so on), the interband response can be tailored to different wavelength regions.

2.9.1. NIR-FIR dualband HIWIP detectors

A NIR-FIR dualband detector based on a *p*-GaAs HIWIP detector has been reported (Ariyawansa *et al.*, 2005). The structure consisted of a bottom contact (p^{++}) layer with 1.0 μm thickness, a barrier layer with 1.0 μm thickness, an emitter (p^{+}) layer with 0.2 μm thickness, and a top contact layer. The spectral response for different bias voltages in both NIR and FIR regions at 4.6 K is given in Fig. 5.19A. The optimum responsivity at 0.8 μm is ~9 A/W while the detectivity is $\sim 2.7\times10^{11}$ Jones under 100 mV reverse bias at 4.6 K. The response because of intraband transition is observed up to 70 μm with a responsivity of ~1.8 A/W and a specific detectivity of $\sim 5.6\times10^{10}$ Jones at 57 μm under 100-mV reverse bias. The sharp drop around 37 μm was assigned to the strong absorption around the reststrahlen band of GaAs and the peaks at 57 and 63 μm were assigned to transitions of impurity atoms in the barrier region (Esaev *et al.*, 2004b). The spectral responsivity curves resulting from both interband and intraband transitions for temperatures from 4.6 K to 20 K are shown in Fig. 5.19B. An optimum responsivity of ~8 A/W and a detectivity of $\sim 6\times10^{9}$ Jones were

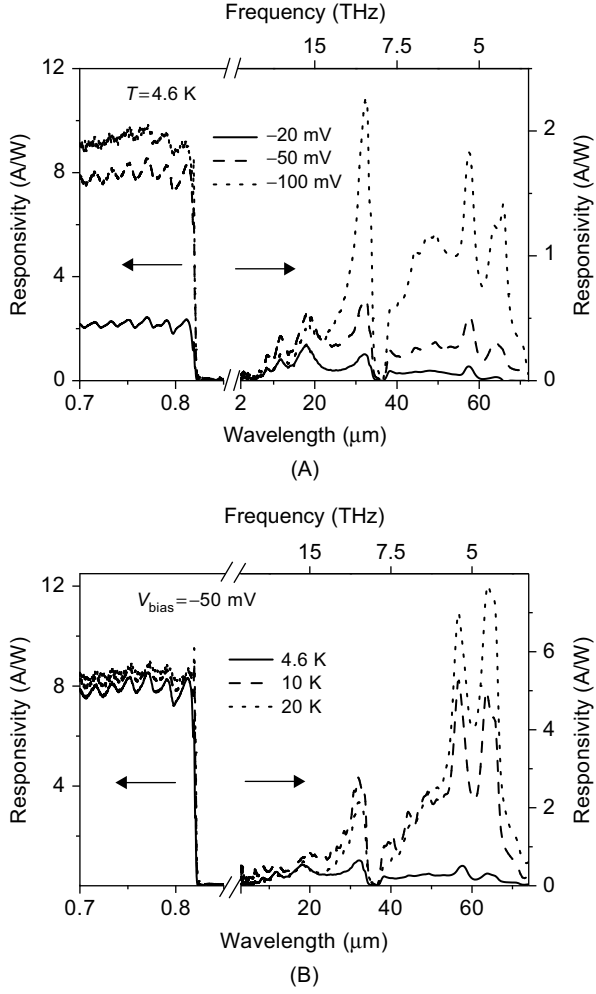

FIGURE 5.19 (A) The interband and intraband response of the GaAs-based HIWIP at 4.6 K under different reverse bias values. (B) Shows both interband and intraband response at different temperatures under −50 mV bias. The left and right axes are corresponding to NIR and FIR responsivity, respectively, and a break on the frequency axis at 39 THz has been made in order to expand the view in both regions.
Reused with permission from Ariyawansa *et al*. (2005). Copyright 2005, American Institute of Physics.

obtained at 0.8 μm for interband response, while a responsivity of ~7 A/W and a detectivity of $\sim 5\times10^{9}$ Jones were reported at 57 μm, under 100-mV reverse bias at 20 K (Ariyawansa *et al.*, 2005).

Following the same principle, a second detector operating in both the NIR and FIR ranges has been reported based on a *p*-type Si HIWIP detector (Ariyawansa *et al.*, 2006b). The NIR response at −1 V bias had a threshold of ∼1.05 μm, agreeing with the ∼1.17 eV bandgap of Si at 4.6 K. A NIR responsivity of 0.024 A/W was obtained at 0.8 μm with a detectivity of $\sim 1.7 \times 10^9$ Jones at 0.8 μm under −1 V bias at 4.6 K. The FIR response is in the range of 5–35 μm. A responsivity of 157 A/W at 25 μm at −2 V bias was reported, which translates to an efficiency-gain product of 7.8.

2.9.2. UV–IR dualband HEIWIP detectors

Recently, a nitride-based dualband detector was also demonstrated which showed response in both the UV and IR ranges (Ariyawansa *et al.*, 2006a; Perera and Matsik, 2007) similar to the previous NIR-FIR detectors as shown in Fig. 5.20, in which a theoretical response is calculated for comparison using a model developed by Matsik and Perera (2008). This detector used interband absorption to detect the UV radiation and intraband absorption to detect the IR radiation. The GaAs was replaced by GaN and the AlGaAs replaced by AlGaN. Although the initial detector using only two contacts required separate modulations to distinguish the UV from the IR, a later design using three contacts and separate active regions for the UV and the IR were able to distinguish UV from IR without separate modulations (Jayasinghe *et al.*, 2008). This approach allows tremendous variations in the thresholds. By using AlGaN in both layers with different

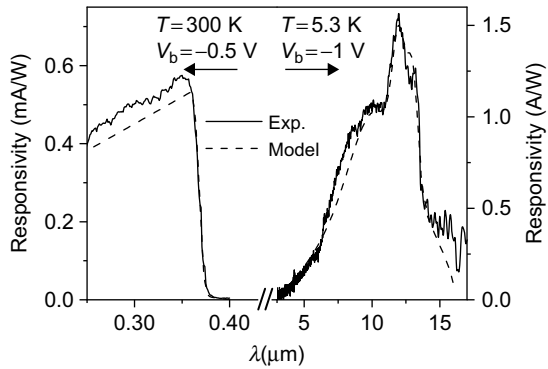

FIGURE 5.20 Calculated UV/IR responses (dashed line) of the detector, fitted with experimental results (solid line). UV response at 300 K and a −0.5 V bias, and response at −1.0 V and 5.3 K. Note that although the response is only shown in the two ranges of interest, the model calculates the response over the entire range from the UV to the IR. Reused with permission from Matsik and Perera *et al.* (2008). Copyright 2008, American Institute of Physics.

Al fractions and adjusting the Al fraction in the barriers, the UV threshold can be tailored, whereas by adjusting the difference between the fractions in the emitters and barriers, the IR threshold can be tailored. However, for high-performance devices, the quality of the GaN/AlGaN material system needs to be improved, which is presently the focus of many researchers.

2.9.3. Simultaneous and separate identification of UV and IR

A three-contact design modification for the UV–IR dual-band detector (one common contact for both regions) allowed separate and simultaneous identification of UV (250–360 nm) and IR (5–14 μm) radiation (Jayasinghe *et al.*, 2008). The structure consists of an n^+-GaN top-contact (TC) layer, an undoped $Ga_{0.974}Al_{0.026}N$ layer acting as the UV-active region, an n^+-GaN middle-contact (MC) layer, the IR-active region, and a bottom-contact (BC) layer. The IR-active region consists of two periods of an n^+-GaN emitter layer and an undoped $Ga_{0.974}Al_{0.026}N$ barrier layer. Depending on the bias either the MC or the BC also acts as an emitter. The dual-band detection is based on two absorption mechanisms in the heterostructure: interband absorption in the top $Ga_{0.974}Al_{0.026}N$ layer for UV response and free-carrier absorption in the emitters for IR response. Figure 5.21 shows the device structure and the band diagram and the schematic of the detector.

Throughout this discussion, the MC terminal is the common terminal for both UV- and IR-active regions. Hence, forward (reverse) bias denotes that the TC for the UV-active region or the BC for the IR-active region is positive (negative) relative to the MC. When the TC is negatively biased, it also acts as an emitter, making the IR detection possible in the UV-active region. This effect can be decreased by reducing the TC layer thickness, which reduces the IR absorption and the generated photocurrent. Furthermore, this TC layer absorbs UV radiation, suppressing the transmission of UV into the UV-active region, without generating a photocurrent because the excited electron–hole pairs are trapped by the barriers and recombine in the highly doped TC. For an optimum UV response, the TC layer thickness was found to be 0.1 μm, which is thin enough to reduce the IR absorption while still giving uniform electric field distribution across the UV-active region. Furthermore, the generation of IR photocurrent is prominent in the IR-active region, while no UV photocurrent is expected irrespective of the bias configuration because almost all the UV radiation is absorbed within the UV-active region.

The spectral response is shown in Fig. 5.22. The solid curves show simultaneously measured photocurrents from the UV-active region (Fig. 5.22A) and the IR-active region (Fig. 5.22B) at 77 K when both IR and UV radiations were incident onto the detector. The dashed curve in Fig. 5.22A represents the photocurrent from the UV active region when only the UV radiation was incident. Comparing the two curves, it is

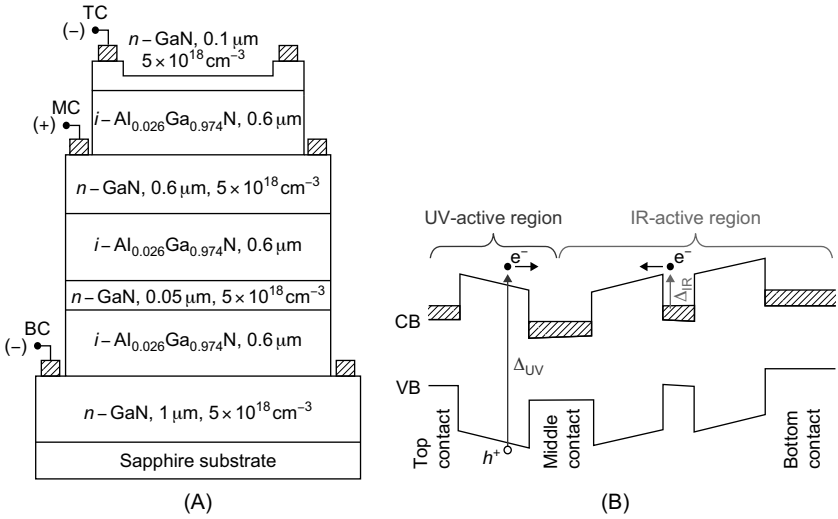

FIGURE 5.21 (A) The three contact structure for simultaneous dual-band response measurements. Three contacts allow separate readouts from the UV- and IR-active regions. The labels TC, MC, and BC indicate the top-, middle-, and bottom-contacts, respectively, and (+) or (−) shows the relative potential at which the device was operated. (B) The band diagram of UV–IR dual-band detectors under reverse bias configuration. CB and VB are the conduction and valance bands, respectively. Three contacts allow separate readouts from the UV- and IR-active regions. Δ_{UV} and Δ_{IR} represent the transition energies for interband and intraband absorption, respectively.

evident that there is no significant effect from IR radiation on the response from the top and middle contacts, indicating the sole UV detection from the UV active region, whereas the response from the IR-active region is because of the fixed IR radiation (9.3 μm), and there is no significant effect from the UV radiation except for a feature at 365 nm, which is probably because of one of the following two reasons: (1) it could be because of a light transmission as a result of a generation–recombination mechanism of an exciton (Jiang *et al.*, 2001). An exciton 365 nm generated in the top GaAlN layer in the UV-active region could relax re-emitting a UV photon, generating another exciton, and so on, allowing a small fraction of photons at 365 nm to pass through to the IR-active region; (2) the low-energy UV radiation that has energy less than the bandgap of $Ga_{0.974}Al_{0.026}N$ was absorbed in the MC layer, and the generated photocurrent could be either due to the minority carrier transportation (Chernyak *et al.*, 2001) in the structure where the generated holes were recombined with the electrons in the valence band, or due to electron hopping from the filled impurity acceptor levels above the valence band of GaAlN layers.

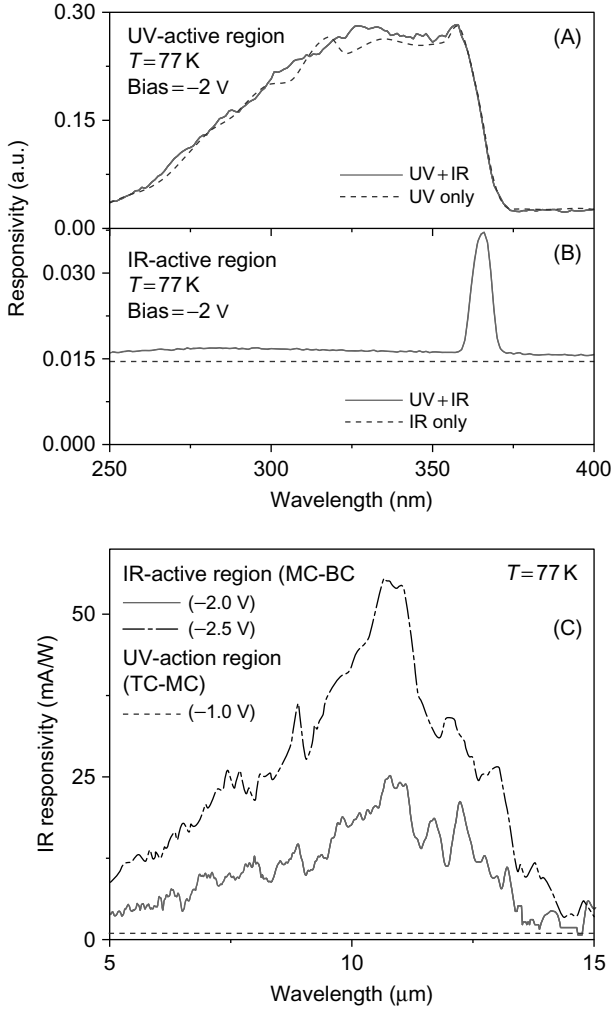

FIGURE 5.22 Simultaneously measured photo currents (solid lines) from (A) UV-active region and (B) IR-active region at 77 K, when both IR and UV radiation were incident onto the detector. The UV wavelength was varied between 250 and 400 nm, while IR was fixed at 9.3 μm (using a CO_2 laser). The dashed line in (A) represents the photocurrent when only UV radiation was incident and the dashed line in (B) indicates the response level (which is constant with time), as a reference level for the "UV + IR" response from the IR-active region, when only IR radiation was incident which only corresponds to the bottom axis. The lower and upper *x*-axes of (A) are also the upper axis of (B). (C) The IR response from IR- and UV-active regions at 77 K. The UV-active region showed almost zero response for IR radiation under reverse bias configuration as expected.
Reused with permission from Ranga C. Jayasinghe, Optics Letters 33, 2422–2424 (2008), Copyright 2008, Optical Society of America.

The broad IR responses from both active regions obtained separately at 77 K are shown in Fig. 5.22C, with the free-carrier response seen as a broad peak with a maximum near 11 μm. The UV-active region did not show a measurable IR response under negative bias but did show a response under positive bias as expected.

The observed response in the GaN/GaAlN single-element detector indicates the capability of simultaneously detecting both the UV and IR responses with near-zero spectral cross talk. The detector can be further improved by the addition of more periods of GaN/GaAlN in the IR-active region.

3. INTER-VALENCE BAND DETECTORS

Room-temperature or thermoelectrically cooled operation of infrared detectors would greatly reduce the weight and/or power requirements and are of importance for various practical applications. In addition to the InSb and PbSe detectors for the 3–5 μm range, HgCdTe (Gordon *et al.*, 2006), quantum well (Alause *et al.*, 2000), quantum dot (Ariyawansa *et al.*, 2007), and type-II strained superlattice (Plis *et al.*, 2007) detectors are being studied as SWIR–LWIR detectors. Infrared detection based on hole transitions from the light/heavy hole (LH/HH) bands to the spin-orbit split-off (SO) band coupled with an interfacial workfunction offers a novel approach for detectors to realize uncooled or near room-temperature operation.

The split-off band detection was initially observed in HEIWIP detectors (Perera *et al.*, 2006). The split-off detection mechanism was then confirmed using detectors specifically designed and grown by MBE, which showed response up to 330 K (Jayaweera *et al.*, 2008). The detectors have a similar structure to the standard HEIWIP detectors consisting of alternating *p*-doped absorbing layers (emitters) and undoped barrier layers sandwiched between two highly doped (1×10^{19} cm^{-3}) top and bottom contact layers with thickness of 0.2 and 0.7 μm, respectively. The standard interfacial workfunction in the HEIWIP detectors will still provide a λ_t. However, this offset (threshold) can be adjusted in comparison with the split-off energy for higher response or higher temperature operation.

The highly doped and thick emitters (18.8 nm) will lead to three-dimensional energy states as opposed to quantized states. An E–*k* band diagram around $k = 0$ in the Brillouin Zone (BZ) for an emitter region is schematically given in Fig. 5.23A and the band diagram for the device is shown in Fig. 5.23B. The SO band is separated from the degenerate point of the LH and HH bands at $k = 0$ by an energy E_{E-SO} which equals the spin splitting energy Δ_{SO}. The detector mechanism consists of three

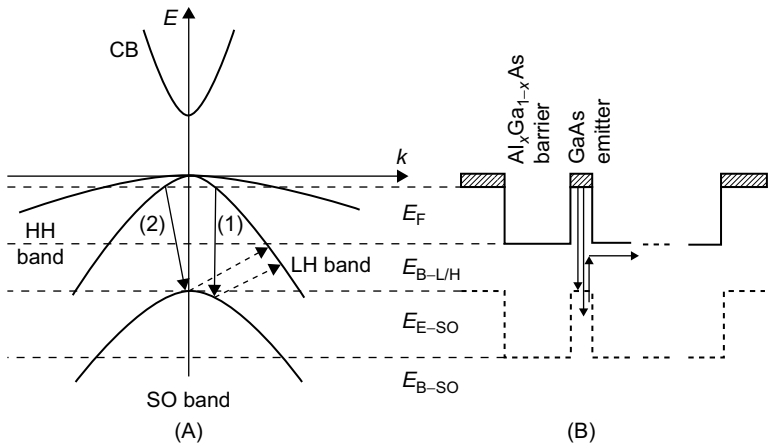

FIGURE 5.23 (A) $E - k$ diagram for an emitter region of the detector and (B) band diagram of the detector structure illustrating the different IR detection threshold mechanisms. The horizontal dashed lines $E_{B-L/H}$ and E_{B-SO} indicate the LH/HH and split-off band maximum ($k = 0$) positions in the barrier. The horizontal dotted lines E_F and E_{B-SO} indicate the Fermi energy and the split-off energy in the emitter at $k = 0$. The arrows indicate the possible threshold transition mechanisms: (1) a direct transition from LH band to SO band followed by scattering back to LH band (2) an indirect transition followed by scattering back to LH band.
Reused with permission from Perera *et al.* (2009).

main steps: (i) photoabsorption, exciting the carriers from the emitters, (ii) escape of the photoexcited carriers, and (iii) the sweep out and collection of the escaped carriers. Photoexcited carriers in the SO band can escape directly or scatter back into the LH/HH bands and then escape. The lowest barrier for the excited carriers in LH/HH bands is the threshold workfunction Δ as defined for HIP detectors which determines the λ_t for free-carrier response and thermionic dark current hence controlling maximum operating temperature. Increasing Δ results in a reduction in the free-carrier response making SO transitions become dominant, but large Δ also decreases the escape probability and gain. The optimum value will be determined by the key application requirement of high operating temperature or high performance. Unlike QWIP detectors, SO detectors will detect normal incidence radiation removing the need for light coupling processes and associated costs.

The spin-orbit splitting effects result from the coupling of electron spin to the orbital angular momentum via the spin-orbit interaction which is a relativistic effect and scales with the atomic number of the atom. Hence spin-split off based IR detection should be sensitive to the magnetic

field allowing magnetic tunability and controllability. For semiconductors containing lighter elements, the splitting energy becomes small hence extending the SO transition wavelength into far-infrared (FIR) spectral region. For example, zincblende or wurtzite crystal structures of GaN having the SO splitting energies of 20 meV(~4.8 THz/62 μm) and 8 meV (~1.92 THz/156 μm), respectively (Levinshtein *et al.*, 2001) would be a promising material for THz detection.

In addition to SO-HH transitions, the selection rule allows hole transitions between the LH and HH bands. These can take place at k values other than the BZ center where the LH-HH energy separation approximately approaches 2/3 of the SO splitting energy. Such a consideration composes a complete scene for inter-valence band absorption (IVBA) in p-type semiconductors. A broad spectral region covering MWIR and LWIR regions can be expected as the LH-HH transition energy has no minimum limitation from the band-structure point of view. Experimental measurements on the absorption properties for p-doped semiconductors have been made over a variety of materials, e.g., GaAs (Braunstein and Magid, 1958; Songprakob *et al.*, 2002; Hu *et al.*, 2005b; Rinzan *et al.*, 2004), GaP (Wiley and DiDomenico, 1971), GaSb (Chandola *et al.*, 2005; Hu *et al.*, 2005a), Ge (Briggs and Fletcher, 1952), InAs (Stern and Talley 1957), InP (Henry *et al.*, 1983), and InSb (Gobeli and Fan, 1960). All these p-type materials show broad absorption extended into the FIR region. The IVBA strength is generally increased with the doping. However, enhanced scattering of carriers by charged centers at higher doping concentrations could relax the selection rule $\Delta k = 0$ leading to broad SO-HH peak and reduced intensity (Newman and Tyler, 1957), whereas the LH-HH peak keeps a well-defined shape even at very high doping concentrations (Songprakob *et al.*, 2002). The energy onset of LH-HH absorption band (e.g., 0.25 eV reported by Braunstein and Magid (1958)) approximately approaches the LH-HH separation $\Delta_1(\Lambda)$ in the $\langle 111 \rangle$ direction (e.g., 0.225 eV reported by Lautenschlager *et al.* (1987)) for p-GaAs. From the band structure point of view, hole transitions will see the parallel structure of the LH and HH bands along $\langle 111 \rangle$ and $\langle 100 \rangle$ directions enhancing the transition rate. The use of detection mechanism involving LH-HH transitions is promising for infrared detection to concurrently cover multiband spectral region by using a single structure, e.g., p-type GaAs/AlGaAs detectors (Lao *et al.*, 2010). However, the background from 300 K-blackbody radiation (peak at ~10 μm) inducing a photocurrent in the p-type GaAs/AlGaAs detector could degrade the detection capability. In this case, it will be desirable to narrow the detection to one specific region, e.g., MWIR. A possible solution is to design the zero-response λ_t to suppress the long-wavelength response. As it will be discussed in Section 3.4, the

use of a cavity structure can also enhance the absorption in the MWIR range.

3.1. Uncooled SO detectors

The split-off band detection was initially observed in the GaAs/AlGaAs HEIWIP detector (Perera *et al.*, 2006) which was designed for the 10–15 μm range with a 20 μm threshold (Matsik *et al.*, 2004). The detector structure was composed of 16 periods of *p*-doped 18.8-nm GaAs emitters doped to 1×10^{18} cm^{-3} and 125-nm $Al_{0.12}Ga_{0.88}As$ barriers. Figure 5.24 presents the spectral responsivity at different temperatures. Also shown is the absorption spectra of *p*-doped $Al_{0.01}Ga_{0.99}As$ films indicating stronger split-off absorption above the free-carrier absorption. It has been observed that optimum response occurs at a moderate temperature, which could be the result of thermal-related phonon effects on the escaping rate for excited carriers and increased dark current at higher temperatures. Optimum

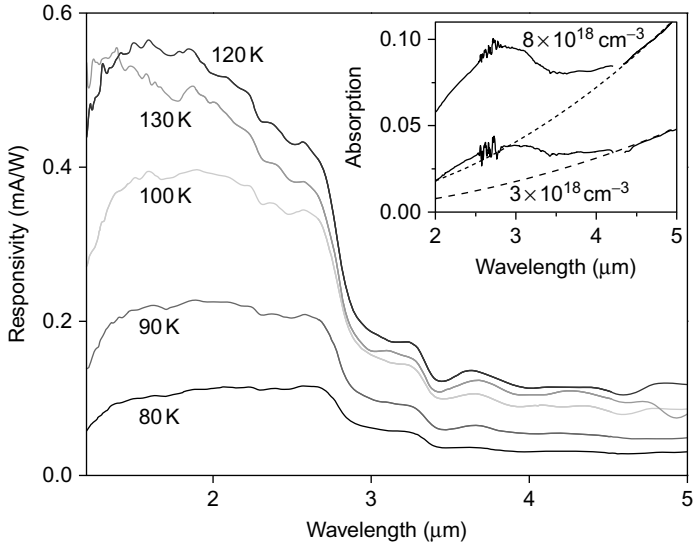

FIGURE 5.24 Measured responsivity of the HEIWIP detector at various temperatures at 5 kV/cm. The inset shows the measured absorption for $Al_{0.01}Ga_{0.99}As$ films. The solid lines are the total absorption in the films, while the dashed lines are the λ^2 curves indicating the free-carrier absorption. The difference represents the absorption from the split-off band. Higher doping leads to a large increase in the split-off absorption as seen from the curves.

Reused with permission from Perera *et al.* (2006). Copyright 2006, American Institute of Physics.

response and the operating temperature are two competing requirements. Smaller Δ giving rise to a longer free-carrier threshold wavelength allows increased collection of the carrier over the split-off barrier, also allowing a higher dark current. In contrast, larger Δ reducing the dark current will lead to an increase in operating temperature but accordingly decreases the photocarrier escape and the response. The two steps seen in the response at 2.8 and 3.4 μm are related to the transitions 1 and 2 as illustrated in Fig. 5.23.

This initial results imply that the SO transition-based mechanism could be a novel approach for infrared detection with the capability of high-operating temperatures. Studies have shown that the inter-valence band absorption including the SO transitions was one critical part of optical loss for long-wavelength semiconductor lasers at elevated temperatures (Henry *et al.*, 1983; Piprek *et al.*, 1996), which is related to the temperature behavior of IVBA resulting from a higher amount of thermally populated heavy holes. In contrast, such IVBA behavior will be beneficial for infrared detectors.

As discussed above, the threshold workfunction Δ (shown in Fig. 5.23) determines the thermionic dark current hence controlling maximum operating temperature. By designing structures with optimized Δ values, high-operating-temperature SO detectors is thus possible. Such design was demonstrated (Jayaweera *et al.*, 2008; Perera and Matsik, 2010) on three detector structures SP1, SP2, and SP3 which have different Δ values of 155, 207, and 310 meV (corresponding Al fractions are $x = 0.28, 0.37, 0.57$), respectively. All these detectors were composed of 3×10^{18} cm^{-3} p-doped 18.8-nm GaAs emitters and 60-nm undoped $Al_xGa_{1-x}As$ barriers. The current voltage (I–V) characteristics were measured with different temperatures from 70 to 300 K. As shown in Fig. 5.25A, dark current density at 1 V bias reached the same order at 140, 190, and 300 K for samples SP1, SP2, and SP3, respectively. The measured dark current densities of SP1, SP2, and SP3 at 150 K temperatures (solid lines) are consistent with a thermionic model (dots) as shown in Fig. 5.25B.

The spectral response of SP1, SP2, and SP3 were measured at temperatures up to 140, 190, and 330 K, respectively, as shown in Fig. 5.26. The maximum responsivity of SP3 was observed at 2.5 μm and 4 V bias above which increased dark current (low-dynamic resistance) decreased the response. The λ_t for the response mechanisms 1 and 2 shown in Fig. 5.23 can be identified in Fig. 5.26 at 2.9 and 3.4 μm, respectively. The higher responsivity was seen for samples (SP1 and SP2) with longer λ_t, possibly because of impact ionization (gain) and collection efficiency, compared with samples with shorter λ_t, as shown in the inset of the Fig. 5.26. Based on the noise measurements, the D^* values are calculated for each sample and listed in Table 5.4.

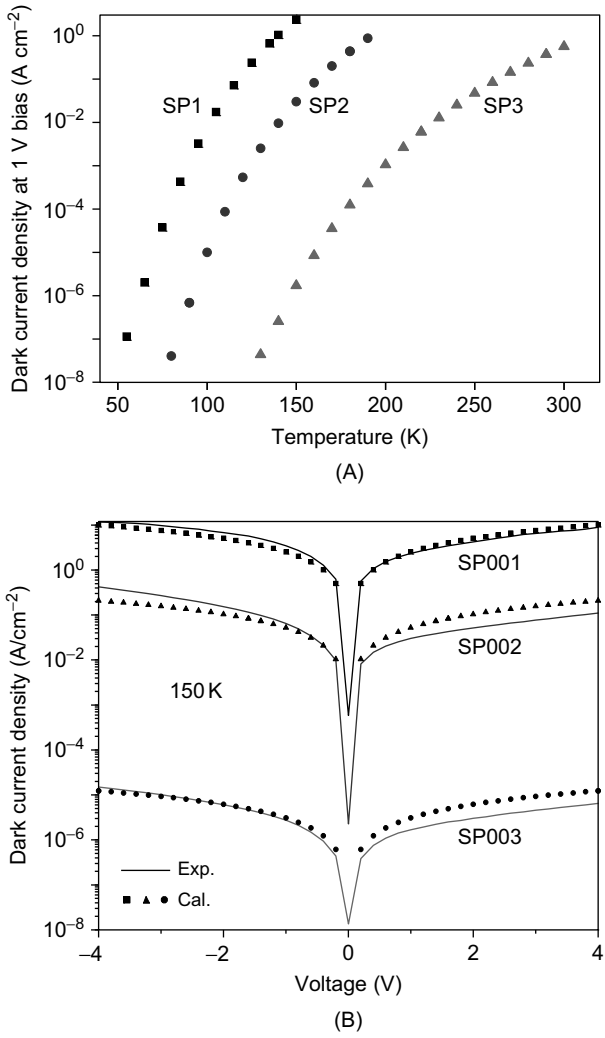

FIGURE 5.25 (A) The dark current density versus temperature for samples SP1, SP2, and SP3 under 1 V applied bias. The dark current densities reached 1 A/cm^2 for each sample at 140, 190, and 300 K. (B) The dark current density for the three samples measured at 150 K showing thermionic emission.
Reused with permission from Perera *et al.* (2009).

Also shown in Fig. 5.26 is a comparison with the model response (Matsik *et al.*, 2009), which gives an agreement with the predicted peak response being within 20% of the measured value for all the biases. The

theoretical analysis gives an understanding to the observed SO response by which related optimization on detector structures can be carried out. The model details will be discussed in Section 3.4.

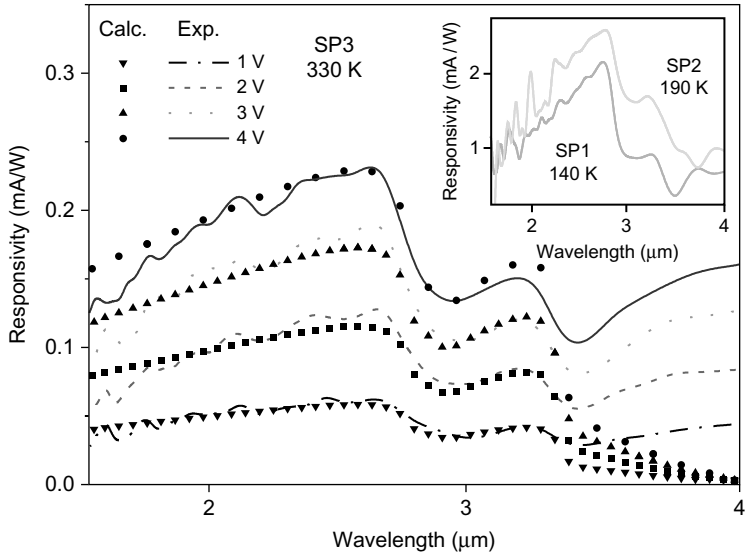

FIGURE 5.26 The measured responsivity of the sample SP3 under four different biases at 330 K. The inset shows the responsivity of the samples SP1 and SP2 at 140 and 190 K, respectively. (Reused with permission from P. V. V. Jayaweera *et al.*, Applied Physics Letters, 93, 021105 (2008).) Copyright 2008, American Institute of Physics. Also shown is the comparison of experimental spectra with the calculated response (Matsik *et al.*, 2009) showing good agreement except at the longer wavelengths. The disagreement at long wavelengths is because of the thermal mechanism that is not included in the model. Reused with permission from Matsik *et al.* (2009). Copyright 2009, American Institute of Physics.

TABLE 5.4 Sample parameters for detectors SP1–3. The dynamic resistance (R_{Dyn}), dark current density (I_{Dark}) at 1 V bias, and D^* are experimentally measured values. $\Delta_{\mathrm{L/H}}$ is the designed band offset

Sample	$\Delta_{\mathrm{L/H}}$ (eV)	$T_{\max}$ (K)	R_{Dyn} (Ω)	I_{Dark} ($\mathrm{A\,cm^{-2}}$)	D^* (Jones)
SP1	0.155	140	787	0.663	2.1×10^6
SP2	0.207	190	913	0.875	1.8×10^6
SP3	0.310	300	1138	0.563	6.8×10^5

3.2. LH-HH transitions for long-wavelength infrared detection

In contrast to the SO transitions that give rise to absorption in the spectral region with photon energy larger than the SO splitting energy, the LH-HH transitions (as one type of IVB transitions) are allowed by the selection rule producing absorption in the MWIR and LWIR region (Lao *et al.*, 2010). A schematic of IVBA processes and room-temperature absorption spectra for *p*-GaAs are shown in Fig. 5.27. The IVBA appears as on top of FCA lines, where the broad peak around 4–16 μm is because of the LH-HH transitions. The broad LH-HH feature is related to two factors contributing to the IVBA strength: the difference in hole distribution functions between the initial and final states relating the Fermi level, and the joint density of states (JDOS) $|\overrightarrow{k} \cdot \nabla_k(E_{ki} - E_{kj})|^{-1}$ (i and j represent band indexes). Because of the parallel structure of LH and HH bands, JDOS shows singularities at

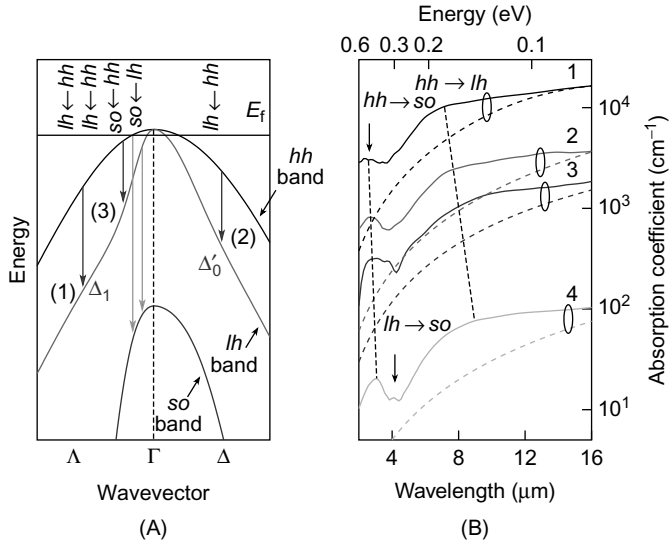

FIGURE 5.27 (A) Schematic of the valence-band structure along the direction of ⟨111⟩ (Λ) and ⟨100⟩ (Δ). Various IVBA transitions are indicated. The (1), (2), and (3) represent LH-HH transitions at different wavevectors. The Fermi level is calculated for 3×10^{18} cm^{-3} *p*-doped GaAs at 80 K. (B) Measured room-temperature absorption spectra of *p*-GaAs compared with the calculated FCA curves plotted by dashed lines. Also shown is data from Songprakob *et al.* (2002) (curve 1) and Braunstein and Kane (1962) (curve 4); the doping levels for curves 1–4 are 2.7×10^{19}, 8.0×10^{18}, 3.0×10^{18}, and 2.7×10^{17} cm^{-3}, respectively.
Reused with permission from Lao, Pitigala *et al.* (2010). Copyright 2010, American Institute of Physics.

large k and hence yields considerable absorption in the short-wavelength part of the LH-HH absorption band.

Because the SO and LH-HH transitions are all IVBA processes occurring in p-type materials, the LH-HH transition-based response can be observed in SO detectors. Figure 5.28 shows the spectral responsivity for detectors with different zero-response threshold (λ_t) and emitter dopings. Sample HE0206 consists of 16 periods of 18.8-nm p-GaAs emitters doped to 1×10^{17} cm^{-3} and 125-nm undoped $Al_{0.12}Ga_{0.88}As$ barriers. Sample 1332 has 12 periodic units with the same thick emitters and barriers as HE0206, but the emitter doping level is at 3×10^{18} cm^{-3} and the Al fraction of barriers is 0.15. The SO-HH transition-based short-wavelength response in samples SP1–3 have been discussed earlier in this section.

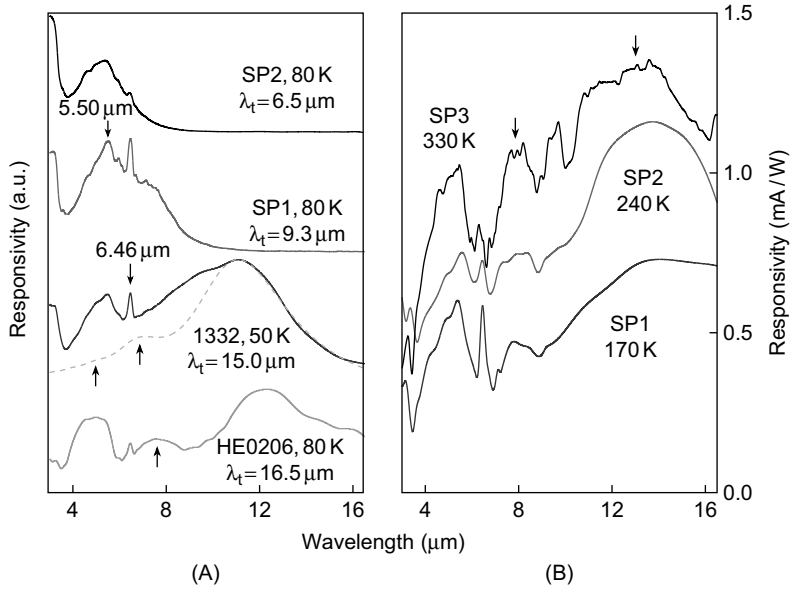

FIGURE 5.28 (A) Spectral response of detectors with different λ_t. The curves from top to bottom are measured at the bias of 8, 2, 1, and 2 V, respectively. In comparison with the FCA response (dashed line) calculated for the detector 1332, LH-HH transitions produce response between 4 and 10 μm. (B) High-operating-temperature capability was measured on samples SP1, SP2, and SP3 under 0.2, 0.3, and 3 V, respectively, showing broad range from 4 to 16.5 μm. The wavelength region above designed threshold is because of a thermal detection mechanism. Cavity interference modes are all marked with the arrows in (A) and (B).

Reused with permission from Lao, Pitigala *et al.* (2010). Copyright 2010, American Institute of Physics.

The detector with long-wavelength threshold in Fig. 5.28 shows a broad response between 4 and 16.5 μm involving the FCA and IVBA contributions together. The FCA response alone can be calculated by the escape cone model (Esaev *et al.*, 2004) in which the escape rate of holes out of the emitter region is determined by the photoemission process. However, thermally assisted tunneling contribution at high biases will mix in this process deteriorating the model accuracy. Therefore, the model FCA response for low biases was calculated and compared with detector 1332 shown Fig. 5.28A. The comparison indicate LH-HH transitions can produce spectral response up to 10 μm. The LH-HH process is rather prominent in terms of similar responsivity features observed in detector HE0206 although its emitters are relatively low doped at 1×10^{17} cm^{-3}. High-operating-temperature capability was measured on detectors SP1, SP2, and SP3 shown in Fig. 5.28B, indicating promising uncooled operation. The range above λ_t could be because of the thermal detection mechanisms. Thermal-related processes such as phonon scattering increase the response time at high temperatures. Hence, an enhanced responsivity was observed at high temperatures when a lower optical-path-difference (OPD) velocity value was used for the FTIR settings. A minimum OPD velocity below which response is nearly unchanged was thus used. The peak at ~13 μm is because of the cavity enhancement of the *p*-GaAs/AlGaAs structure.

In the LH-HH response region, two peaks determined by their center positions at 5.50 and 6.46 μm were observed. Their corresponding energy values (0.225 and 0.192 eV, respectively) are matched with reported LH-HH separations along the Λ and Δ directions, respectively, e.g., $\Delta_1(\Lambda) = 0.224$ eV as reported by Lautenschlager *et al.* (1987) and $\Delta_0^{'}(\Delta) = 0.193$ eV as reported by Zollner (2001). Therefore, hole transitions at points in $\overrightarrow{k}$ space along the Λ and Δ directions are the reason for this result.

The LH-HH transition-based concept builds up the factors including the split-off mechanism and the FCA for GaAs being a platform to realize multispectral infrared detection in an internal photoemission detector. In comparison with MCT detectors which have been realized for uncooled operation within the 2–16 μm spectral range and are commercially available (Rogalski, 2005), the discussed GaAs-based device will be a viable alternative with the robustness of the III–V material system. Uncooled operation is also possible for this type of device which is promising for applications where detecting high-intensity radiation is required.

3.3. SO-HH transitions for spectral response extension

As the SO splitting energy scales with the atomic number of the atom, extended spectral response range can be achieved by using different materials. For the wavelength range in the 3–5 and 8–14 μm atmospheric

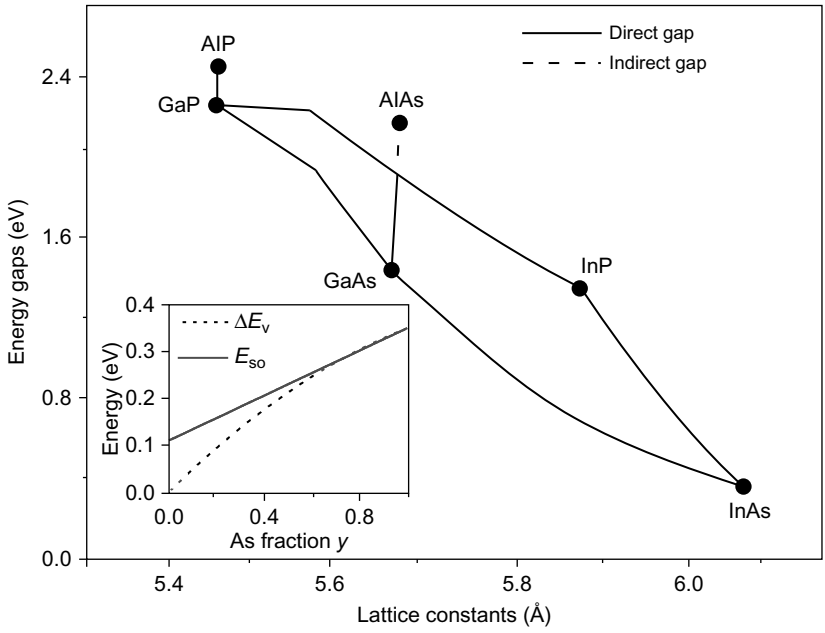

FIGURE 5.29 Band gap and lattice constant of selected III–V semiconductors (data were taken from Levinshtein *et al.* (1996)). Solid lines represent direct band region and dashed lines represent indirect band region. GaP/AlGaP would be a high-quality, lattice-matched system similar to GaAs/AlGaAs. Also, InGaAs and InGaP can be lattice-matched to InP and GaAs, respectively. The inset shows the variation of the valence band offset energy (ΔE_v) and split-off energy (E_{SO}) of the $In_{1-x}Ga_xAs_yP_{1-y}$/InP heterostructure with As fraction y, where $x = 0.47y$.
Reused with permission from Perera *et al.* (2009).

windows arsenide and phosphide would be the best materials because their split-off energies fall in this range. A bandgap versus lattice constant plot of selected arsenide and phosphide materials is shown in Fig. 5.29. The use of $GaAs_{0.4}P_{0.6}$ is possible for a full coverage of 3–5 μm range as its split-off threshold is near 5 μm; however, the lattice mismatch with the GaAs substrate is an issue for high-quality epitaxy. The GaP and AlP have the lattice constant at 5.4505 and 5.4510 Å (Levinshtein *et al.*, 1996), respectively, and thus the $Al_xGa_{1-x}P$ ternary alloy is naturally lattice matched with the GaP substrate. A SO detector with GaP emitter and $Al_xGa_{1-x}P$ barrier will give rise to 80 meV (16 μm) of split-off threshold energy (wavelength). Growth of $Al_xGa_{1-x}P$-based structures should not be difficult because characteristics of GaP/AlGaP heterojunctions (Adomi *et al.*, 1992), superlattice (Nabetani *et al.*, 1995), heterostructure-based detectors (Prutskij *et al.*, 1995), and solar cells (Sulima *et al.*, 2003) have already been reported.

$In_{1-x}Ga_xAs_yP_{1-y}$ can be lattice matched to InP when $x = 0.47y$. The SO splitting energy can be tuned from 0.11 to 0.379 eV (3.3–11 μm) by changing the As alloy fraction y from 0 to 1 ($\Delta_{SO} = 0.11 + 0.24y$; Yamazoe *et al.*, 1981). Because the valence band discontinuity of the $In_{1-x}Ga_xAs_yP_{1-y}$/InP heterostructure can be expressed as (Levinshtein *et al.*, 1996) $\Delta E_v = 0.502y - 0.152y^2$, the free-carrier threshold wavelength will also be tunable. By setting y within 0.5–0.7 range, the ΔE_v will correspond to a λ_t in the 4–5 μm range. The calculated ΔE_v and Δ_{SO} for different As fractions y is shown in the inset of Fig. 5.29.

Another potential application of the SO detection mechanism is to develop detectors for the THz range. The extending of SO response toward THz frequency domain can be possibly achieved by zincblende or wurtzite crystal structures of GaN that have the SO splitting energies of 20 meV(~4.8 THz/62 μm) and 8 meV (~1.92 THz/156 μm), respectively (Levinshtein *et al.*, 2001). Using the model reported by Matsik *et al.* (2009) as developed for GaAs/AlGaAs SO detectors (see Fig. 5.26), a preliminary calculation (Perera *et al.*, 2009) was applied to zincblende crystal *p*-GaN/AlGaN split-off band detector in Fig. 5.30A which responds up to 4.2 THz as shown in Fig. 5.30B. In comparison with the BiB detectors in this wavelength range which operate at low-temperatures (Table 5.1), the calculation indicates relatively high-temperature operation could be achieved using the SO detection mechanism.

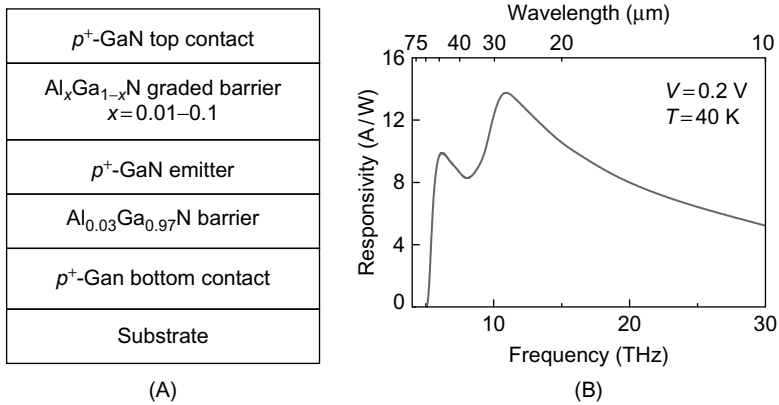

FIGURE 5.30 (A) Schematic diagram of a preliminary structure of a GaN/AlGaN split-off band detector. The thickness of the emitter and barrier layers are 20 and 400 nm, respectively. The doping concentration of the emitter and contact layers is 1×10^{19} cm^{-3}. (B) Theoretically predicted response based on the model reported by Matsik *et al.* (2009). The threshold at 4.2 THz (62 μm) corresponds to the split-off energy (~20 meV) of *p*-GaN.

3.4. Modeling and optimization of SO detectors

The transport of carriers in the detector involves a series of processes: the excitation of carriers by incident light, the escape over the barriers, and the trapping and refilling injection of carriers. A high quantum efficiency would be expected by increasing the escaping rate while reducing the trapping. Because a detector generally includes multiple emitters to enhance the absorption, a design with each emitter contributing to the response should result in high performance. Therefore, it will be desirable to understand and explain the response observed in detectors mentioned above from a theoretical point of view, in order to improve the performance. In this section, a theoretical analysis on the SO detectors is presented. The model response shows consistency with the measured response. Detector optimization is then suggested based on the model results. Also an analysis on the dark current concerning the electrical uniformity and the absorption enhancement using an optical cavity is presented.

3.4.1. Graded barriers and resonant escape

To optimize the SO response, a theoretical modeling has been carried out by Matsik *et al.* (2009). The calculated responsivity agrees with the predicted peak response being within 20% of the measured value for all the biases as shown in Fig. 5.26. The model involves five steps in the calculations: (1) the absorption in the emitters, (2) the transport of excited carriers to the emitter/barrier interface, (3) the escape probability at the emitter/barrier interface, (4) the capture rate for injected carriers in the emitters, and (5) the dark and photocurrents. In the transport of injected or photo/thermal-excited carriers throughtout the device, various scattering events can occur. A scattering event can cause the transferring of a carrier from one energy state to another which could result in escape over high-energy barrier or capture into low-energy states. Holes excited from the LH/HH bands into the SO band can move forward the emitter/barrier interface by remaining within the same (SO) band or scattering back into the LH/HH bands and then escape at the interface, contributing to the photo current for SO response. In this modeling, three basic scattering processes are considered: (1) ionized impurity scattering, (2) phonon scattering, and (3) hot/cold carrier scattering.

As a preliminary to the model, the energy bands for the emitter layers were calculated using an eight-band $\boldsymbol{k} \cdot \boldsymbol{p}$ approach (Kane, 1966) to calculate the absorption and scattering rates for the various mechanisms. The IR absorption in the emitter layer consists of two components, a direct absorption involving only the photon and the hole, and an indirect absorption involving an additional scattering through phonon or impurity to conserve momentum. The two processes could be calculated separately and

then combined to give the total absorption. The ionized impurity scattering should be significant only in the emitters, and it will be calculated (Brudevoll *et al.*, 1990) including the effects of screening on the scattering rates. The phonon scattering rates will be calculated (Scholz, 1995), including the absorption and emission of both optical and acoustic phonons for transitions both within and between the hole bands.

The total escape probability for the photoexcited carriers can be obtained using a Monte Carlo method. The photoexcitation is obtained using the rates for transitions at a specific value of k. A carrier is randomly selected from the excited carrier distribution and made to propagate forward toward the emitter–barrier interface, which is assumed to travel in a straight line until scattered, or to reach the interface. At the interface, the carrier either escapes or is reflected. There are two possible escape mechanisms: (1) direct escape over the barrier while remaining in the same hole band as presently occupied, where the probability can be determined using an escape cone model (Esaev *et al.*, 2004a) or (2) for the carrier to transfer into a different band as it crosses the emitter/barrier interface. This is possible as a result of the mixing that occurs between the light, heavy, and split-off hole states. The motion of the carrier is followed until it either escapes or has an energy level less than that of the barrier when it is retained in the emitter.

This model was tested by comparing the calculated results with experimental measurements for detector SP3 as shown in Fig. 5.26. The results gave reasonable agreement with measured responsivity. The deviation seen at long wavelengths beyond $\sim 3.5\,\mu m$ appears to be because of a thermal detection mode that is also present, which is not included in the modeling. Because the model response reasonably agrees with the experiments, structure optimizing can be carried out by varying the structural parameters used in the model such as the barrier height, the doping, and the thickness of emitters. The model gives a photocurrent gain of 0.95 ± 0.05 which is in agreement with the predicted value of 1.0 (Shen and Perera, 1998) for a single emitter detector with all the injected current being trapped in the emitter. This theoretical analysis suggested that modifications in the design to activate more emitters would lead to increase gain hence improved response, which can be achieved by grading the top barrier in order to produce an offset between the barriers on the two sides of the emitter. The improved responsivity with increasing barrier offset is shown in Fig. 5.31A. Another potential improvement is the use of a double-barrier structure to increase escape of holes from the split-off to the light/heavy hole bands by bringing the two bands into resonance. Other parameters, such as the doping level, parameters related to antireflection coatings, and so on, can be also optimized using the model results as shown in Table 5.5 and Fig. 5.31B.

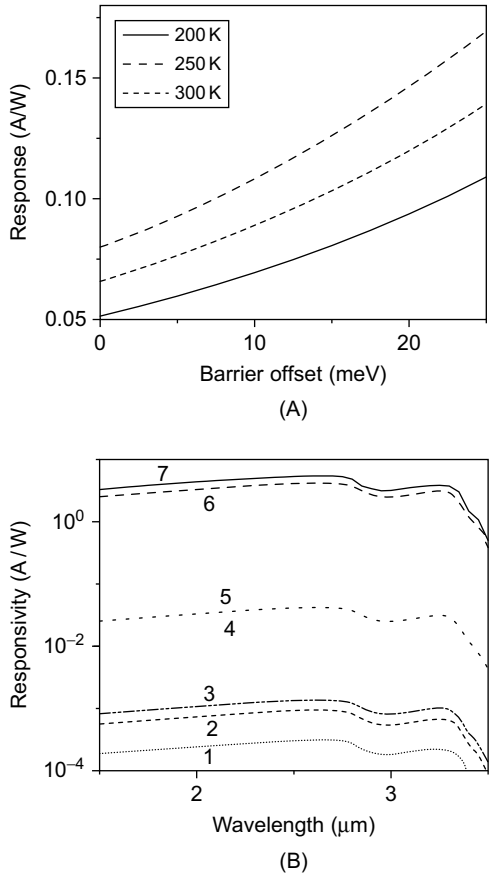

FIGURE 5.31 (A) The calculated responsivity variation with barrier offset for a detector with a free-carrier threshold of 4 μm at three different temperatures at a bias of 1.0 V. Reused with permission from Matsik *et al.* (2009). Copyright 2009, American Institute of Physics. (B) The predicted improvement in responsivity of a GaAs/AlGaAs detector as different design modifications are incorporated. The GaAs-based design consisted of 30 periods of $3 \times 10^{18}\,\mathrm{cm}^{-3}$ p-doped 18.8-nm GaAs emitters and 60-nm $Al_xGa_{1-x}As$ barriers. Table 5.5 indicates the modifications for each curve and their effects on responsivity. Each curve includes the effects of all modifications for the curves with lower numbers. Curves 3 and 4 have the same responsivity.

3.4.2. Resonant cavity enhancement

Because the optical thickness of the structure is comparable with or greater than the operating wavelength (e.g., p-GaAs for MIR detection based on SO-HH transition and for LWIR detection based on LH-HH transitions), embedding the active region in a Fabry–Perot (F–P) resonant cavity can

TABLE 5.5 Design modifications and improvement in SO detector performance where the curve number corresponds to that in Fig. 5.31B

Curve	Modifications	Responsivity	
		Improvement factor	Value (mA/W)
1	Measured results		0.14
2	Increase doping from 3×10^{18} to 10^{19} cm^{-3}	$\times 3$	0.42
3	Barrier offset of 100 meV	$\times 1.5$	0.64
4	Graded barrier offset of 50 meV	$\times 1$	0.64
5	Increase effective multiple emitters to 30	$\times 30$	19
6	Resonant escape of carriers	$\times 100$	1900
7	Antireflection coatings	$\times 1.3$	2500

enhance the performance by increasing the optical absorption (Selim Ünlü and Strite, 1995; Korotkov *et al.*, 2001; Esaev *et al.*, 2003). The F–P cavity can be fabricated by applying a metallic mirror on one side of the structure with the semiconductor/air interface as another mirror. Such a detector has been realized in experiments for a QWIP (Shen *et al.*, 2000). Similarly, this idea can be applied to the *p*-GaAs detector under discussion.

For comparison between different cavity designs, all calculations were made to detectors with the incoming light from the bottom. In this case, a gold film could be deposited on the device surface as the top mirror. Based on an optical transfer-matrix method, cavity optimization on the absorption enhancement was evaluated through calculating the ratio of total squared electric field in emitter layers to that of the incoming light. Results are shown in Fig. 5.32. As the high-reflection wavelength range of the gold film is broad, an overall enhancement can be observed in both the MWIR and LWIR region. However, such improvement could be undesirable for *p*-GaAs detectors. As mentioned before, unnecessary noise is resulted because of response from other regions (e.g., LWIR) if the detector is specifically designed for MWIR detecting. Thus, it will be desirable to narrow the spectral detection. Increasing the barrier height to reduce λ_t can be one of methods. Another option is to use an F–P cavity with a localized enhancement region. As shown in Fig. 5.32A, a distributed Bragg reflector (DBR) consisted of alternating layers with equal optical thickness ($\lambda_0/4$), but different refractive index can produce a high-reflection range centered at the wavelength λ_0. By using DBR in place of the gold mirror, cavity enhancement localized around λ_0 was obtained as seen in curve (III) (Fig. 5.32B). A further enhancement is also possible by using another GaAs/AlGaAs DBR as the bottom mirror. The increase in the reflectivity of the top mirror enhances the standing wave inside the F–P cavity and hence the absorption. However, the full-width at half-maximum (FWHM) is drastically reduced, creating sharp peaks as seen in Fig. 5.32C. Also shown is a structure with two GaAs/$Al_{0.5}Ga_{0.5}As$ DBRs (curve V).

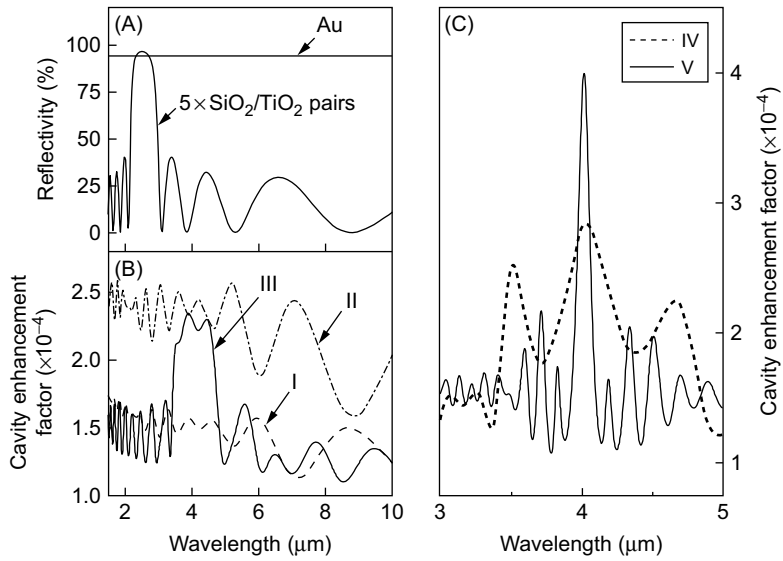

FIGURE 5.32 Comparison of calculated cavity-enhancement factors for detector SP3. The cavity-enhancement factor is defined as the total squared electric field for the emitter layers to the incoming light. Curve (I) represents the calculated result for detector SP3 without cavity enhancement, (II) for the structure to optimize SP3 by depositing a gold top mirror, (III) for the structure with a five-pair SiO_2/TiO_2 top DBR, (IV) for the structure with a five-pair SiO_2/TiO_2 top DBR and a one-pair $GaAs/Al_{0.9}Ga_{0.1}As$ bottom DBR, and (V) for the structure with a 20-pair $GaAs/Al_{0.5}Ga_{0.5}As$ top DBR and a five-pair $GaAs/Al_{0.5}Ga_{0.5}As$ bottom DBR. All calculations assume the light is incoming from the bottom side of the device. This configuration will facilitate the fabrication of metallic (gold) or dielectric (SiO_2/TiO_2) mirrors. A comparison of reflection spectra between the gold film and a five-pair SiO_2/TiO_2 DBR is shown in (A), indicating localized high-reflection wavelength region was obtained using a DBR. The use of two DBRs drastically narrows the enhancement peak with which only one cavity mode can be possible selected, e.g., curve (V) in (C).

The $Al_{0.5}Ga_{0.5}As$ DBR has a narrower high-reflection wavelength region than that of SiO_2/TiO_2 and $GaAs/Al_{0.9}Ga_{0.1}As$ DBRs. Therefore, only one cavity mode (~4 μm) can be selectively enhanced. In summary, the above-mentioned theoretical calculation schematically shows the idea of cavity enhancement either for the overall spectral region or for a specific wavelength range.

3.4.3. Dark current analysis

As the SO detectors work at high temperatures, increased thermal emission currents could bring about the issue of electrical uniformity because

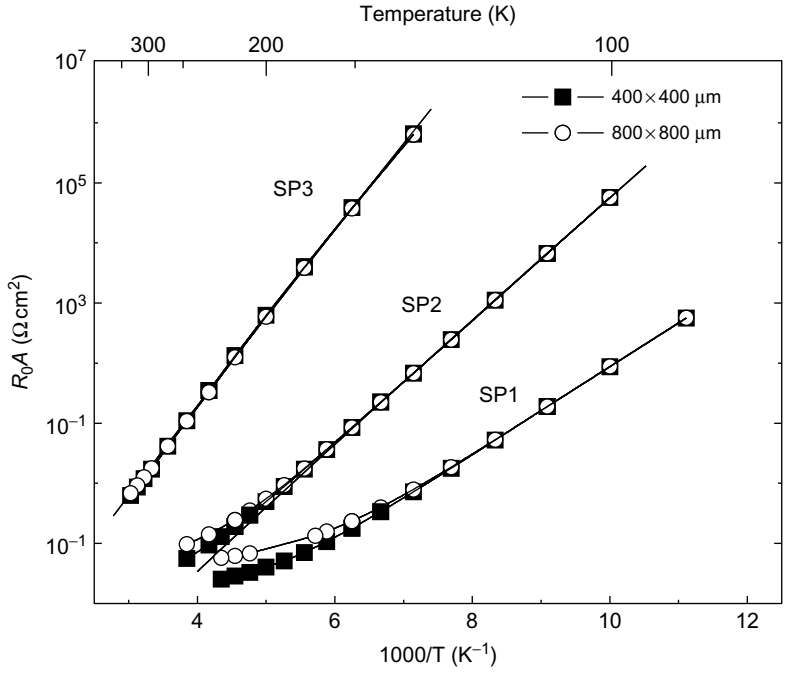

FIGURE 5.33 Temperature-dependent R_0A for detectors SP1–3. The solid square and hollow circle are the experimental data for square-mesa devices with sizes of 400 and 800 μm, respectively. A fit to the low-temperature region (solid line) based on thermionic currents is extended to compare R_0A deviation at high temperatures. Reused with permission from Lao, Jayaweera *et al.* (2010), IEEE Copyright 2010.

of the device configuration under discussion (square mesa with ring metal contacts) (Lao *et al.*, 2010). The temperature-dependent zero-bias differential resistance (R_0A) extracted from the current–voltage–temperature (I–V–T) measurements are plotted in Fig. 5.33 for detectors SP1–3. The cross-sectional geometry area was used to calculate R_0A. The low-temperature R_0A was fitted (solid lines) by using a thermal emission model. Higher R_0A values than the fitting curves for detectors SP1 and SP2 indicates the actual conduction area has reduced at high temperatures. The temperature effects can be related to a conductivity ratio of the vertical component to the lateral: $\alpha = \overline{\sigma}_z/\overline{\sigma}_x$ where $\overline{\sigma}_z$ and $\overline{\sigma}_x$ are the averaged vertical and lateral component of conductivity, respectively. The $\overline{\sigma}_x$ shows temperature dependence through hole mobility, while the $\overline{\sigma}_z$ is determined by the thermal current across the potential barrier with an exponential behavior over the temperatures. Therefore, α also shows an exponential increase with temperatures as shown in Fig. 5.34A, which is consistent with the R_0A deviation. A clear understanding of this electrical

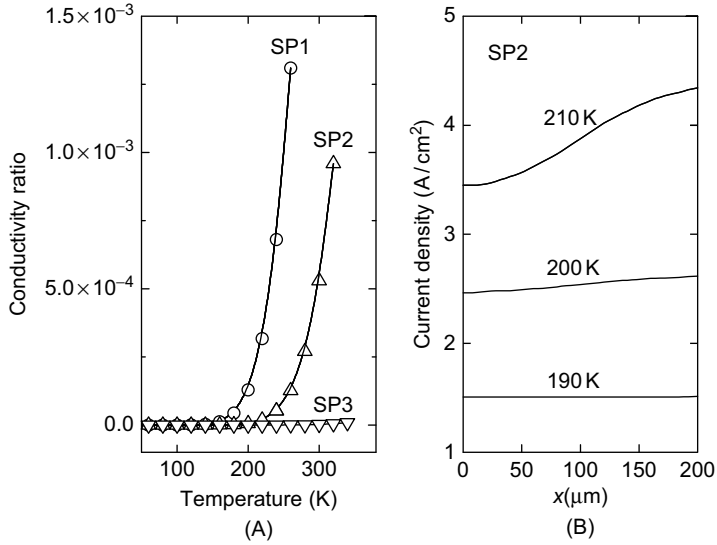

FIGURE 5.34 (A) The calculated conductivity ratio α as a function of operating temperatures. (B) The calculated lateral current distribution for detector SP2 with the mesa 400×400 μm at 190, 200, and 210 K, respectively. $x = 0$ represents the device center. The nonuniformity becomes remarkable when the temperature is increased.

characteristics is to numerically calculate the 2-D current distribution based on the α-T relationship in Fig. 5.34A. The vertical current at the interface between the active region and the bottom contact layer for the sample SP2 was calculated as a function of lateral position x, and shown in Fig. 5.34B. Obviously, the current localization is induced at temperatures more than 190 K. Analysis suggests that high-energy barrier can efficiently reduce the issue of current localization. The detector SP3 shows uniform electrical performance for room-temperature operation. Also better electrical uniformity can be attained in detectors with smaller mesas.

4. CONCLUSION

A schematic diagram indicating the spectral response ranges and the peak responsivity values of the internal photoemission detector structures (BIB, HIWIP, HEIWIP, SO, QWIP, QDIP, QRIP) discussed in this chapter is shown in Fig. 5.35. In this figure, the solid lines represent the full response wavelength ranges for each detector, while the peak response wavelengths are indicated by the symbols. The Ge:Ga BIB detector having a λ_t of 220 μm was reported by Watson *et al.* (1993). An AlGaAs emitter–based terahertz HEIWIP detector, which has a threshold of 128 μm (2.3 THz), was reported

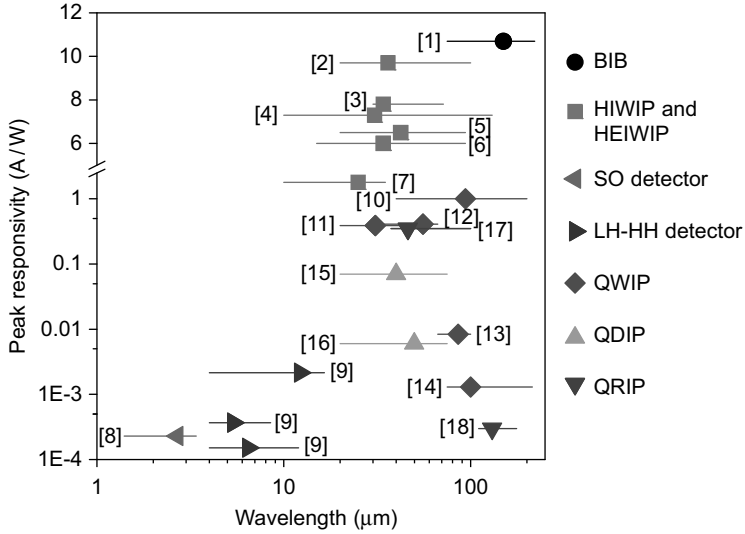

FIGURE 5.35 Summary of the response for different reported detectors. The vertical axis gives the peak responsivity for each detector. The horizontal solid lines represent the response range (ends corresponding to zero-response threshold), while the symbols represent the peak response wavelength. The detectors used in this figure are listed below with their operating temperature (the temperature at which the data was reported at T), reported maximum operating temperature ($T_{\max}$), and BLIP temperature (T_{BLIP}). [1]: Ge:Ga BIB ($T = 1.7\,\text{K}$), Watson *et al.* (1993); [2]: p-GaSb-HIWIP ($T = 4.9\,\text{K}$, $T_{\max} = 15\,\text{K}$), Jayaweera *et al.* (2007); [3]: p-GaAs HIWIP ($T = 4.2\,\text{K}$), Esaev *et al.* (2004b); [4]: p-AlGaAs HEIWIP ($T = 4.8\,\text{K}$, $T_{\text{BLIP}} = 20\,\text{K}$), Rinzan *et al.* (2005b); [5]: n-GaAs HEIWIP ($T = 6\,\text{K}$, $T_{\max} = 25\,\text{K}$), Weerasekara *et al.* (2007); [6]: p-GaAs HEIWIP ($T = 4.2\,\text{K}$), Matsik *et al.* (2003); [7] p-Si HIWIP ($T = 4.6\,\text{K}$, $T_{\text{BLIP}} = 25\,\text{K}$, $T_{\max} = 30\,\text{K}$), Ariyawansa *et al.* (2006b); [8]: SO detector ($T = 330\,\text{K}$), Jayaweera *et al.* (2007); [9]: LH-HH detecors ($T = 8\,\text{K}$), Lao *et al.* (2005); [10]: QWIP ($T = 8\,\text{K}$, $T_{\text{BLIP}} = 12\,\text{K}$), Luo *et al.* (2005); [11]: QWIP ($T = 8\,\text{K}$, $T_{\text{BLIP}} = 17\,\text{K}$), Luo *et al.* (2005); [12]: QWIP ($T = 8\,\text{K}$, $T_{\text{BLIP}} = 13\,\text{K}$), Luo *et al.* (2005); [13]: QCL-like QWIP ($T = 10\,\text{K}$, $T_{\max} = 50\,\text{K}$), Graf *et al.* (2004); [14]: QWIP ($T = 3\,\text{K}$), Patrashin and Hosako (2008); [15]: QDIP ($T = 80\,\text{K}$, $T_{\max} = 120\,\text{K}$), Huang *et al.* (2008); [16]: T-QDIP ($T = 80\,\text{K}$, $T_{\max} = 150\,\text{K}$), Su *et al.* (2005); [17]: quantum dot infrared photodetector (QDIP; $T = 4.2\,\text{K}$, $T_{\max} = 80\,\text{K}$), Huang *et al.* (2009); [18]: quantum ring infrared photodetector (QRIP; $T = 8\,\text{K}$, $T_{\text{BLIP}} = 50\,\text{K}$), Lee *et al.* (2009). The QDIP and QRIP data are reported here for comparison.

by Rinzan *et al.* (2005b). Other HIWIPs and HEIWIPs are based on the work reported by Jayaweera *et al.* (2007), Esaev *et al.* (2004b), Weerasekara *et al.* (2007), Matsik *et al.* (2003), and Ariyawansa *et al.* (2006b). The detectors using IVBA mechanisms are based on the work reported by Jayaweera *et al.* (2008) and Lao *et al.* (2010).

In conclusion, detectors with spectral response as long as ~220 μm have been reported in BIB detectors and HIWIP detectors (Perera *et al.*, 1992). However, one of the drawbacks associated with BIB detectors is that they require very high quality materials in the barrier in order to achieve the best performance. Also, BIB detectors' response range is material specific unlike other detectors. AlGaAs/GaAs HEIWIP detectors have shown a broad response with a threshold at 130 μm, while the IVB detectors discussed in this chapter are actually a type of HEIWIP with a detection mechanism based on IVBA processes. The use of this mechanism provides a novel approach realizing uncooled or near room-temperature operation by which greatly reduced weight and/or power requirements are of importance for practical applications.

5. NOMENCLATURE

2D	two dimensional
3D	three dimensional
BIB	blocked-impurity-band
BLIP	background limited infrared performance
BZ	Brillouin Zone
CB	conduction band
C-V-T	capacitance voltage temperature
D^*	specific detectivity
DWELL	dots-in-a-well
FCA	free-carrier absorption
FIR	far infrared (30–100 μm)
FPA	focal plane array
f	frequency
f_t	threshold frequency
FTIR	Fourier Transform Infrared
g	photoconductive gain
η	quantum efficiency
HEIWIP	Heterojunction Interfacial Workfunction Internal Photoemission
HIP	Heterojunction/Homojunction Internal Photoemission
HIWIP	Homojunction Interfacial Workfunction Internal Photoemission
IR	infrared
IVB	inter-valence-band
IVBA	inter-valence-band absorption
I–V–T	current voltage temperature
IWIP	Interfacial Workfunction Internal Photoemission
JDOS	joint density of states

Jones	units of specific detectivity, $\mathrm{cm}\sqrt{\mathrm{Hz}}/\mathrm{W}$
λ	wavelength
λ_p	peak wavelength
λ_t	threshold wavelength
LWIR	long-wavelength infrared (5–14 μm)
MBE	molecular beam epitaxy
MWIR	midwavelength infrared (3–5 μm)
NIR	near infrared (0.8–5 μm)
SO	Split-off
SWIR	short-wavelength infrared (3–5 μm)
T	operating temperature
T_{max}	maximum operating temperature
T_{BLIP}	background limited infrared performance temperature
THz	terahertz, 10^{12} Hz
T-QDIP	tunneling quantum dot infrared photodetector
UV	ultraviolet
VB	valence band
VLWIR	very-long-wavelength infrared (14–30 μm)

ACKNOWLEDGMENTS

This work was supported in part by the U.S. NSF Grant Nos. ECS-0553051 and U.S. Army Grant No. W911NF-08-1-0448. The authors acknowledge the contributions of Dr H. C. Liu and his group at NRC, Canada, Prof. P. Bhattacharya and his group at the University of Michigan, Prof. S. Krishna and his group at the University of New Mexico, Prof. V. I. Gavrilenko and his group at Institute for Physics of Microstructures, Russia, Prof. E. Linfield and his group at the University of Leeds, United Kingdom, and Prof. Yossi Paltiel and his group at Hebrew University of Jerusalem, Israel. Important contributions made by Dr Ian Ferguson's group at Georgia Institute of Technology, Dr N. Dietz's group at Georgia State University, Dr S. G. Matsik at NDP Optronics, LLC and the past and present members of the Optoelectronics Laboratory at Georgia State University are also acknowledged. Some of the work reported here were carried out under the support from U.S. Air Force (SBIR and STTR awards to NDP Optronics LLC) and the Georgia Research Alliance. Special thanks are due to Dr Yan-feng Lao and Dr Gamini Ariyawansa for manuscript preparation.

REFERENCES

Adomi, K., Noto, N., Nakamura, A., and Takenaka, T. (1992). *J. Cryst. Growth* **124**, 570.

Alause, H., Knap, W., Robert, J. L., Planel, R., Thierry-Mieg, V., Julien, F. H., Zekentes, K., and Mossed, V. (2000). *Semicond. Sci. Technol.* **15**, 724–727.

Ariyawansa, G., Perera, A. G. U., Su, X. H., Chakrabarti, S., and Battacharya, P. (2007). *Infrared Phys. Technol.* **50**, 156–161.

Ariyawansa, G., Rinzan, M. B. M., Alevli, M., Strassburg, M., Dietz, N., Perera, A. G. U., Matsik, S. G., Asghar, A., Ferguson, I. T., Luo, H., Bezinger, A., and Liu, H. C. (2006a). *Appl. Phys. Lett.* **89**, 091113.

Ariyawansa, G., Rinzan, M. B. M., Esaev, D. G., Matsik, S. G., Hastings, G., Perera, A. G. U., Liu, H. C., Zvonkov, B. N., and Gavrilenko, V. I. (2005). *Appl. Phys. Lett.* **86**, 143510–3.

Ariyawansa, G., Rinzan, M. B. M., Matsik, S. G., Hastings, G., Perera, A. G. U., Liu, H. C., Buchanan, M., Sproule, G. I., Gavrilenko, V. I., and Kuznetsov, V. P. (2006b). *Appl. Phys. Lett.* **89**, 061112–3.

Ariyawansa, G., Rinzan, M. B. M., Strassburg, M., Dietz, N., Perera, A. G. U., Matsik, S. G., Asghar, A., Ferguson, I. T., Luo, H., and Liu, H. C. (2006c). *Appl. Phys. Lett.* **89**, 141122–3.

Bandaru, J., Beeman, J. W., Haller, E. E., Samperi, S., and Haegel, N. M. 2002. *Infrared Phys. Technol.* **43**, 353–360.

Bardeen, J. (1956). *Nobel Prize Lecture* 318–341.

Beeman, J. W., Goyal, S., Reichertz, L. A., and Haller, E. E. (2007). *Infrared Phys. Technol.* **51**, 60–65.

Blakemore, J. S. (1982). *J. Appl. Phys.* **53**, R123–R181.

Briggs, H. B., and Fletcher, R. C. (1952). *Phys. Rev.* **87**, 1130–1131.

Braunstein, R., and Magid, L. (1958). *Phys. Rev.* **111**, 480–481.

Braunstein, R., and Kane, E. O. (1962). *J. Phys. Chem. Solids* **23**, 1423–1431.

Brudevoll, T., Fjeldly, T. A., Baek, J., and Shur, M. S. (1990). *J. Appl. Phys.* **67**, 7373.

Cardozo, B. L., Reichertz, L. A., Beeman, J. W., and Haller, E. E. (2005). *Infrared Phys. Technol.* **46**, 400–407.

Case, T. W. (1917). *Phys. Rev.* **9**(4), 305310.

Chandola, A., Kim, H. J., Dutta, P. S., Guha, S., Gonzalez, L., and Kumar, V. (2005). *J. Appl. Phys.* **98**, 093103–7.

Chernyak, L., Osinsky, A., and Schultea, A. (2001). *Solid-State Electron.* **45**, 1687.

Cho, A. Y. (1979). *J. Vac. Sci. Technol.* **16**, 275–284.

Dumke, W. P. (1983). *J. Appl. Phys.* **54**, 3200–3202.

Einstein, A. (1905). *Ann. Physik* **17**, 132.

Ershov, M., and Liu, H. C. (1999). *J. Appl. Phys.* **86**, 6580–6585.

Esaev, D. G., Matsik, D. G., Rinzan, M. B. M., Perera, A. G. U., and Liu, H. C. (2003). *J. Appl. Phys.* **93**(4), 1879–1883.

Esaev, D. G., Rinzan, M. B. M., Matsik, S. G., and Perera, A. G. U. (2004a). *J. Appl. Phys.* **96**, 4588–4597.

Esaev, D. G., Rinzan, M. B. M., Matsik, S. G., Perera, A. G. U., Liu, H. C., Zvonkov, B. N., Gavrilenko, V. I., and Belyanin, A. A. (2004b). *J. Appl. Phys.* **95**, 512–519.

Escher, J. S. (1981). in: "Semiconductors and Semimetals," edited by Willardson, R. K. and Beer, A. C., Academic Press, New York, p. 195.

Gobeli, G. W., and Fan, H. Y. (1960). *Phys. Rev.* **119**, 613–620.

Graf, M., Scalari, G., Hofstetter, D., Faist, J., Beere, H., Linfield, E., Ritchie, D., and Davies, G. (2004). *Appl. Phys. Lett.* **84**, 475–477.

Haller, E. E., and Beeman, J. W. (2002). in: Proc. Far-IR, Sub-mm, & Millimeter Detector Technology Workshop, NASA CP-211408, paper 2-06.

Harmon, E. S., Melloch, M. R., and Lundstrom, M. S. (1994). *Appl. Phys. Lett.* **64**, 502–504.

Henry, C., Logan, R., Merritt, F., and Luongo, J. (1983). *IEEE J. Quantum Electron.* **19**, 947–952.

Herschel, W. (1800). *Phil. Trans. Roy. Soc. London* **90**, 255.

Hu, Z. G., Perera, A. G. U., Paltiel, Y., Raizman, A., and Sher, A. (2005a). *J. Appl. Phys.* **98**, 023511.

Hu, Z. G., Rinzan, M. B. M., Matsik, S. G., Perera, A. G. U., Winckel, G. Von, Stintz, A., and Krishna, S. (2005b). *J. Appl. Phys.* **97**, 093529.

Huang, G., Guo, W., Bhattacharya, P. Ariyawansa, G., and Perera, A. G. U. (2009). *Appl. Phys. Lett.* **94**, 1011153.

Huang, G., Yang, J., Bhattacharya, P., Ariyawansa, G., and Perera, A. G. U. (2008). *Appl. Phys. Lett.* **92**, 011117–3.

Jain, S. C., Mertens, R. P., and Van, R. J. O. (1991). "Advances in Electronics and Electron Physics." Academic Press, New York.

Jain, S. C., and Roulston, D. J. (1991). *Solid-St. Electron.* **34**, 453–465.

Jantsch, O. (1987). *IEEE Trans. Electron Devices* **34**, 1100–1115.
Jayasinghe, R. C., Ariyawansa, G., Dietz, N., Perera, A. G. U., Matsik, S. G., Yu, H. B., Ferguson, I. T., Bezinger, A., Laframboise, S. R., Buchanan, M., and Liu, H. C. (2008). *Opt. Lett.* **33**(21), 2422–2424.
Jayaweera, P. V. V., Matsik, S. G., Perera, A. G. U., Liu, H. C., Buchanan, M., and Wasilewski, Z. R. (2008). *Appl. Phys. Lett.* **93**, 021105–3.
Jayaweera, P. V. V., Matsik, S. G., Perera, A. G. U., Paltiel, Y., Sher, A., Raizman, A., Luo, H., and Liu, H. C. (2007). *Appl. Phys. Lett.* **90**, 111109–3.
Jiang, H., Zhao, G. Y., Ishikawa, H., Egawa, T., Jimbo, T., and Umeno, M. (2001). *J. Appl. Phys.* **89**, 1046.
Johnson, T. H. (1983). *SPIE Proc. Infrared Detectors* **443**, 60.
Kane, E. O. (1966). in: "Semiconductors and Semimetals." edited by Willardson, R. K. and Bee A. C., Academic Press, New York.
Kane, M. J., Millidge, S., Emeny, M. T., Lee, D., Guy, D. R. P., and Whitehouse, C. R. (1992). in: "Intersubband Transitions in Quantum Wells." edited by Rosencher, E., Vinter, B., and Levine, B. F., Plenum, New York, p. 31–42.
Klauder, J. R. (1961). *Ann. Phys.* **14**, 43–76.
Klein, M. V., and Furtac, T. E. (1986). "Optics." Wiley, New York.
Korotkov, A. L., Perera, A. G. U., Shen, W. Z., Herfort, J., Ploog, K. H., Schaff, W. J., and Liu, H. C. (2001). *J. Appl. Phys.* **89**(6), 3295–3300.
Kosonocky, W. F. (1992). *SPIE* **1685**, 2–19.
Kruse, P. W. (1981). in: "Semiconductors and Semimetals." edited by Willardson, R. K. and Beer, A. C., Academic Press, New York, **18**, 1–20.
Lao, Y. F., Jayaweera, P. V. V., Matsik, S. G., Perera, A. G. U., Liu, H. C., Buchanan, M., and Wasilewski, Z. R., 2010. *IEEE Trans. Electron Devices* **57**, 1230–1236.
Lao, Y. F., Pitigala, P. K. D. D. P., Perera, A. G. U., Liu, H. C., Buchanan, M., Wasilewski, Z. R., Choi, K. K., and Wijewarnasuriya, P. (2010). *Appl. Phys. Lett.* **97**, 091104–3.
Lautenschlager, P., Garriga, M., Logothetidis, S., and Cardona, M. (1987). *Phys. Rev. B* **35**, 9174–9189.
Lee, J.-H., Dai, J.-H., Chan, C.-F., and Lee, S.-C., (2009). *IEEE Photonics Technol. Lett.* **21**, 721723.
Levine, B. F. (1993). *J. Appl. Phys.* **74**, R1–R81.
Levinstein, H. (1965). *Appl. Opt.* **4**(6), 639–647.
Levinshtein, M. E., Rumyantsev, S. L., and Shur, M. S. (1996). "Handbook Series on Semiconductor Parameters." World Scientific, Singapore, New Jersey.
Levinshtein, M. E., Rumyantsev, S. L., and Shur, M. S. (2001). "Properties of Advanced Semiconductor Materials GaN, AlN, InN, BN, SiC, SiGe." John Wiley & Sons, Inc., New York.
Lin, T. L., and Maserjian, J. (1990). *Appl. Phys. Lett.* **57**, 1422–1424.
Liu, H. C., Noel, J.-P., Li, L., Buchanan, M., and Simmons, J. G. (1992). *Appl. Phys. Lett.* **60**, 3298–3300.
Luo, H., Liu, H. C., Song, C. Y., and Wasilewski, Z. R. (2005). *Appl. Phys. Lett.* **86**, 231103–3.
Luo, M. Y., Bosman, G., Van Der Ziel, A., and Hench, L. L. (1988). *IEEE Trans. Electron Devices* **35**, 1351–1356.
Manasevit, H. M. (1968). *Appl. Phys. Lett.* **12**(4), 156–159.
Matsik, S. G., Jayaweera, P. V. V., Jayasinghe, R. C., Perera, A. G. U., Choi, K. K., and Wijewarnasuriya, P. (2009). *J. Appl. Phys.* **106**, 1064503.
Matsik, S. G., Rinzan, M. B. M., Esaev, D. G., Perera, A. G. U., Liu, H. C., and Buchanan, M. (2004). *Appl. Phys. Lett.* **84**, 3435–3437.
Matsik, S. G., Rinzan, M. B. M., Perera, A. G. U., Liu, H. C., Wasilewski, Z. R., and Buchanan, M. (2003). *Appl. Phys. Lett.* **82**, 139–141.
Matsik, S. G., and Perera, A. G. U. (2008). *J. Appl. Phys.* **104**, 044502.

Mooney, J. M., and Silverman, J. (1985). *IEEE Trans. Electron Devices* **32**, 33–39.
Moore, W. J., Freitas, J. A., and Molnar, R. J. (1997). *Phys. Rev. B* **56**, 12073–12076.
Nabetani, Y., Wakahara, A., and Sasaki, A. (1995). *Mater. Sci. Eng. B* **35**, 454–458.
Newman, R., and Tyler, W. W. (1957). *Phys. Rev.* **105**, 885–886.
Patrashin, M., and Hosako, I. (2008). *Opt. Lett.* **33**, 168–170.
Perera, A. G. U. **(**2001). in: "Handbook of Thin Film Devices: Semiconductor optical and Electro optical Devices." edited by Perera, A. G. U., Liu, H. C., and Francombe, M. H., Academic Press, New York.
Perera, A. G. U., Choe, W. J., Francombe, M. H., Sherriff, R. E., and Devaty, R. P. (1993). Superlattices Microstruct. **14**, 123.
Perera, A. G. U., and Matsik, S. G. (2007). Heterojunction Far Infrared Detector. U. S. Patent No. 7253432.
Perera, A. G. U., and Matsik, S. G. (2010). High Operating Temperature SPLIT-OFF Band Infrared Detectors. U. S. Patent No. 7786508. Issued on Aug. 31.
Perera, A. G. U., Matsik, S. G., Jayaweera, P. V. V., Tennakone, K., Liu, H. C., Buchanan, M., Winckel, G. Von, Stintz, A., and Krishna, S. (2006). *Appl. Phys. Lett.* **89**, 131118–3.
Perera, A. G. U., Matsik, S. G., Rinzan, M. B. M., Weerasekara, A., Alevli, M., Liu, H. C., Buchanan, M., Zvonkov, B., and Gavrilenko, V. (2003). *Infrared Phys. Tech.* **44**, 347–353.
Perera, A. G. U., Matsik, S. G., Yaldiz, B., Liu, H. C., Shen, A., Gao, M., Wasilewski, Z. R., and Buchanan, M. (2001). *Appl. Phys. Lett.* **78**, 2241–2243.
Perera, A. G. U., and Shen, W. Z. (1999). *Opto-Electron. Rev.* **7**, 153–180.
Perera, A. G. U., Shen, W. Z., Liu, H. C., Buchanan, M., Tanner, M. O., and Wang, K. L. (1998). *Appl. Phys. Lett.* **72**, 2307–2309.
Perera, A. G. U., Sherriff, R. E., Francombe, M. H., and Devaty, R. P. (1992). *Appl. Phys. Lett.* **60**, 3168–3170.
Perera, A. G. U., Yuan, H. X., and Francombe, M. H. (1995). *J. Appl. Phys.* **77**, 915–924.
Petroff, M. D., and Stapelbroek, M. G. (1986). Blocked Impurity Band Detectors. U. S. Patent No. 4, 568, 960.
Piprek, J., Babic, D. I., and Bowers, J. E. (1996). *Appl. Phys. Lett.* **68**, 2630–2632.
Plis, E., Rodriguez, J. B., Kim, H. S., Bishop, G., Sharma, Y. D., Dawson, L. R., Krishnaa S., Lee S. J., Jones C. E., and Gopal, V. (2007). *Appl. Phys. Lett.* **91**, 133512–3.
Prutskij, T. A., Andreev, V. M., and Larionov, V. R. (1995). *Solar Energy Materials and Solar Cells* **37,** 349–355.
Reichertz, L. A., Beeman, J. W., Cardozo, B. L., et al. (2006). *Millimeter and Submillimeter Detectors and Instrumentation for Astronomy* III. 6275: 62751S-8.
Reichertz, L. A., Cardozo, B. L., Beeman, J. W., et al. (2005). *Infrared Spaceborne Remote Sensing*, pp. 58830Q1-8. SPIE.
Rinzan, M. B. M., Esaev, D. G., Perera, A. G. U., Matsik, S. G., Von Winckel, G., Stintz, A., and Krishna, S. (2004). *Appl. Phys. Lett.* **85**, 5236–5238.
Rinzan, M. B. M., Perera, A. G. U., and Matsik, S. G. (2005a). *Infrared Phys. and Tech.* **47**, 188–194.
Rinzan, M. B. M., Perera, A. G. U., Matsik, S. G., Liu, H. C., Wasilewski, Z. R., and Buchanan, M. (2005b). *Appl. Phys. Lett.* **86**, 071112–3.
Rogalski, A. (2005). *Rep. Prog. Phys.* **68**, 2267.
Scholz, R. (1995). *J. Appl. Phys.* **77**, 3219.
Sclar, N. (1976). Infrared Phys. **16**(4), 435–448.
Shen, A., Liu, H. C., Gao, M., Dupont, E., Buchanan, M., Ehret, J., Brown, G. J., and Szmulowicz, F. (2000). *Appl. Phys. Lett.* **77**(15), 2400.
Shen, W. Z., Perera, A. G. U. (1998). *J. Appl. Phys.* **83**(7), 3923–3925.
Shen, W. Z., Perera, A. G. U., Francombe, M. H., Liu, H. C., Buchanan, M., and Schaff, W. J. (1998). *IEEE Trans. Electron Devices* **45**, 1671–1677.

Shen, W. Z., Perera, A. G. U., Liu, H. C., Buchanan, M., and Schaff, W. J. (1997). *Appl. Phys. Lett.* **71**, 2677–2679.
Shepherd, F. D., Vickers, V. E., and Yang, A. C. (1971). Schottky barrier photodiode with degenrate semiconductor active region. U. S. Patent No: 3,603,847.
Shepherd, F. D. (1992). *Proc. SPIE* **1735**, 250–261.
Shklovskii, B. I. (1980). *Solid State Commun.* **33**, 273–276.
Songprakob, W., Zallen, R., Tsu, D. V., and Liu, W. K. (2002). *J. Appl. Phys.* **91**, 171–177.
Stern, F., and Talley, R. M. (1957). *Phys. Rev.* **108**, 158–159.
Sze, S. M. (1981). "Physics of Semiconductor Devices." John Wiley & Sons, New York.
Szmulowicz, F., and Madarasz, F. L. (1987). *J. Appl. Phys.* **62**, 2533–2540.
Su, X., Chakrabarti, S., Bhattacharya, P., Ariyawansa, G., and Perera, A. G. U. (2005). *IEEE J. Quan. Elec.* **41**, 974–979.
Tohyama, S., Teranishi, N., Konuma, K., Nishimura, M., Asai, K., and Oda, E. (1991). *IEEE Trans. Electron Devices* **38**, 1136–1140.
Tsaur, B. Y., Chen, C. K., and Marino, S. A. (1991). *Proc. SPIE* **1540**, 580–595.
Ünlü, M. S., and Strite, S. (1995). *J. Appl. Phys.* **78**(2), 15.
Vickers, V. E. (1971). *Appl. Opt.* **10**, 2190–2192.
Watson, D. M., Guptill, M. T., Huffman, J. E., Krabach, T. N., Raines, S. N., and Satyapal, S. (1993). *J. Appl. Phys.* **74**, 4199.
Watson, D. M., and Huffman, J. E. (1988). *Appl. Phys. Lett.* **52**, 1602–1604.
Weerasekara, A., Rinzan, M., Matsik, S., Liu, H. C., Buchanan, M., Winckel, G. V., Stintz, A., Krishna, S., and Perera, A. G. U. (2007). *Opt. Lett.* **32**, 1335–1337.
Wiley, J. D., and DiDomenico Jr., M. (1971). *Phys. Rev. B* **3**, 375–385.
Williams, R. (1970). in: "Semiconductors and Semimetals." Vol. 6, edited by Willardson, R. K. and Beer, A. C., Academic Press, New York, p. 97.
Yamazoe, Y., Nishino, T., and Hamakawa, Y. (1981). *IEEE J. Quantum Electron.* **17**, 139–144.
Zhang, Y. H., Luo, H. T., and Shen, W. Z. (2002). *J. Appl. Phys.* **91**, 5538–5544.
Zhang, Y. H., Luo, H. T., and Shen, W. Z. (2003). *Appl. Phys. Lett.* **82**, 1129–1131.
Zollner, S. (2001). *J. Appl. Phys.* **90**, 515–517.